Application of Solid-State Laser to Preparation of Oxide Superconductor Films: Texture Analysis and Critical-Current Performance for Wire Processing

G.I.P. De Silva

Doctor of Philosophy

Department of Environmental System Engineering
Kochi University of Technology
Kochi, Japan

August 2009

Application of Solid-State Laser to Preparation of Oxide Superconductor Films: Texture Analysis and Critical-Current Performance for Wire Processing

G.I.P. De Silva

A dissertation submitted to

Kochi University of Technology

in partial fulfilment of the requirements

for the degree of

Doctor of Philosophy

Department of Environmental System Engineering
Kochi University of Technology
Kochi, Japan

August 2009

Acknowledgment

Initially, I would like to offer my deepest gratitude to my supervisor Prof. T. Maeda for his guidance, support and encouragement. Thanks are extended to Prof. Y. Yoshida and Dr. Y. Ichino of Nagoya University and Prof. Doi of Kagoshima University for their assistance in measuring current characteristics and supportive advices. I thank to Prof. Matsumoto and Prof. Kusukawa, examiners of the final defense, for their valuable comments. It is great pleasure to thank my co-supervisors, Prof. Monma and Prof. Taniwaki of Kochi University of Technology.

In addition to that, I like to express my thanks to Prof. Taniwaki for his assistance in providing X-Ray diffractometer and Scanning Electron Microscope (SEM). It is a pleasure to thank all undergraduate and postgraduate students of the Materials Science Laboratory, Kochi University of Technology for their support during every phase of my research. I appreciate and thank to Prof. Hunter for his valuable advises in writing research papers.

I am also grateful to all doctoral students in our study room, who worked with me over the years. They extended fullest support to succeed my work and their friendship and kindness made me happy. At the same time I thank to all of IRC members, secretaries of Environmental System Engineering Department of KUT, you gave me various supports over these three years.

At last but not least, it is indeed to thank my mother and father for their encouragement, support and sacrifice.

Indika De Silva

Department of Environmental System Engineering,

Kochi University of Technology

Content

Acknowledgement I

Content II

List of Figures and Tables VI

1 Introduction 1

1.1 Background and Objectives of the Work 2

1.2 Other Thin Film Deposition Methods 5

1.2.1 Metal Organic Chemical Vapor Deposition (MO-CVD) 5

1.2.2 Metal Organic Deposition using Trifluoroacetates (TFA-MOD) 7

1.2.3 Sol - Gel Method 8

1.2.4 Molecular Beam Epitaxy (MBE) 9

1.2.5 Sputter Deposition 10

1.2.6 Co-evaporation 12

1.3 Substrate Materials used for Thin Film Deposition 14

1.3.1 Substrate Requirements 14

1.3.2 Different Types of Substrates 15

1.4 Film Nucleation and Growth 18

1.4.1 Three-Dimensional Island Growth 20

1.4.2 Two-Dimensional Full-Mono-Layer Growth 20

1.4.3 Growth of Mono-Layers Followed by Three-Dimensional Islands 21

1.5 Pinning Improving Methods 23

1.5.1 Columnar Defects via Heavy Ion Irradiation 25

1.5.2 Introducing Nano-rods 26

1.5.3 Introducing Second Phase Nano-particles 28

1.5.4 Substrate Surface Decoration 29

1.5.5 Low-Temperature Growth (LTG) Process for $Sm_{1+x}Ba_{2-x}Cu_3O_{7-\delta}$ Films. 30

1.5.6 Replacement of Y with Other RE Elements 31

1.6 References 33

2 Nd:YAG Laser and Pulsed Laser Deposition 37

2.1 Nd:YAG Laser 38

2.1.1 Theory of Operation 38

2.1.2 Advantages of Nd: YAG Laser 39

2.1.3 Model LS-2147 Pulsed Nd:YAG Laser Deposition Machine 39

2.2 Pulsed Laser Deposition Process 41

2.2.1 Laser -Target Interaction 47

2.2.2 Effects of Process Parameters 49

2.2.3 Comparison of PLD with Other Methods 52

2.3 References 53

3 Texture and Surface Morphology of (Y,Ho)BCO Films on MgO Substrates 55

3.1 Experimental Procedures 56

3.1.1 Preparation of $(Y_{1-x}Ho_x)BCO$ Targets

3.1.2 Examination of Y:Ho Ratio Dependence of Lattice Constants 56

3.1.2.1 X-ray Powder Diffraction (XRD: θ-2θ scan) 58

3.1.3 Measuring Laser (FH) Energy Density (E_d) 59

3.1.4 Preparation of Substrates for Deposition 59

3.1.5 Film Deposition by PLD 59

3.1.6 Studying the Effect of Substrate Temperature on Texture

Quality 60
3.1.6.1 Analyzing the c-axis Orientation 60
3.1.6.2 Analyzing the In-plane Texture. 61
3.1.7 Studying the Influence of T-S Distance and Oxygen Pressure on Texture Quality 62
3.1.8 Studying the Influence of T-S Distance and Energy Density on Texture Quality 62
3.1.9 Observation of Surface Morphology 63
3.2 Results and Discussion 65
3.2.1 Y:Ho Ratio Dependence of Lattice Constants 65
3.2.2 Texture Quality of $(Y,Ho)Ba_2Cu_3O_z$ Films 66
3.2.3 Influence of Interrelation of T-S Distance and Oxygen Pressure on Texture Quality 69
3.2.4 Influence of Interrelation of T-S Distance and Energy Density on Texture Quality 70
3.2.5 Examination of Surface Morphology 72
3.3 References 76

4 Current Characteristics of (Y,Ho)BCO Films on STO Substrates 78
4.1 Experimental Procedures 79
4.1.1 Analyzing the Texture Quality 79
4.1.2 Conducting the Oxygen Annealing Treatment 79
4.1.3 Measuring the Critical Temperature (T_c) 80
4.1.4 Measuring the Critical Current (I_c) 84
4.1.5 Observation of Film Cross –Section 85
4.2 Results and Discussion 87

4.2.1 Texture Quality 87
4.2.2 Critical Temperature Measurements 90
4.2.3 Critical Current Density Measurements 94
4.3 References 96

5 Conclusions and Future Prospects 97

List of Figures

Figure 1.1: Principle of MO-CVD process 6

Figure 1.2: Basic Sputter Deposition 11

Figure 1.3: Principle of thermal co- evaporation 13

Figure 1.4: Schematic diagram of atomic processes in the nucleation of 3-D Clusters 20

Figure 1.5: Schematic view of magnetic vortices in superconductor 23

Figure 1.6: AFM images recorded on etched surfaces of BSCCO single crystals that were irradiated with 276 MeV Ag^{2+} ions to produce columnar defect densities of 1.5 x 10^7 defects per square centimeter 25

Figure 1.7: Magnified cross-sectional TEM image of YBCO film with $BaZrO_3$ nanorods 27

Figure 1.8: SEM image of (Y211$_{\sim 1.1\ nm}$/Y123$_{\sim 12.6\ nm}$) × 25 multilayer film. White image nanoparticles have average particle size 14.8±0.7 nm and areal number density ~1.1 ×10^{11} particles cm^{-2} 28

Figure 1.9: Schematic drawing of the LTG-SmBCO thin film inferred from microstructural observations based on the TEM-EDX analysis 31

Figure 2.1: Model LS-2147 pulsed Nd:YAG laser deposition machine 41

Figure 2.2: Optical diagram of the laser cavity 44

Figure 2.3: Principle of pulsed laser deposition 46

Figure 2.4: A schematic drawing of the orientational behaviour depending on the surface mobility of adatoms 52

Figure 3.1: Model JEOL JDX-3500 X-ray diffractometer 57

Figure 3.2: In-plane mis-oriented grains 60

Figure 3.3: Simple side view of YBCO crystal structure 61

Figure 3.4: X-Ray Diffractometer used for in-plane texture assessment 61

Figure 3.5: Model JEOL JSM-5310 Scanning Electron Microscope (SEM) 64

Figure 3.6: Y/Ho ratio dependence of lattice constants 66

Figure 3.7: XRD: θ-2θ scan for sample x= 0.3 67

Figure 3.8: XRD ϕ-scan profiles for samples of x=(a) 0, (b) 0.3, (c) 0.5, (d) 0.7 and(e) 1. prepared on MgO single crystal substrates 68

Figure 3.9: Influence of (a) d_{TS} and p and (b) d_{TS} and E on the texture quality 71

Figure 3.10: SEM image of surface morphology for sample x= 0 73

Figure 3.11: SEM image of surface morphology for sample x= 0.3 74

Figure 3.12: SEM image of surface morphology for sample x= 0.5 74

Figure 3.13: SEM image of surface morphology for sample x= 0.7 75

Figure 3.14: SEM image of surface morphology for sample x= 1 75

Figure 4.1: Annealing profile - PLD chamber 80

Figure 4.2: Current and voltage terminals of sample 81

Figure 4.3: Setting of sample to supply current and voltage 82

Figure 4.4: Resistivity measuring machine 83

Figure 4.5: Schematic drawing of patterned sample 84

Figure 4.6: Model JSM-740IF Field Emission Scanning Electron Microscope (FE-SEM) 86

Figure 4.7: XRD: θ-2θ scan for sample x= 0.3 88

Figure 4.8: XRD ϕ-scan profile for sample of x= 0.3 prepared on STO single crystal substrate 89

Figure 4.9: Temperature dependence of resistivity for sample x=0 90

Figure 4.10: Temperature dependence of resistivity for sample x=0.3 91

Figure 4.11: Temperature dependence of resistivity for sample x=0.5 91

Figure 4.12: Temperature dependence of resistivity for sample x=0.7 92

Figure 4.13: Temperature dependence of resistivity for sample x=1 92

Figure 4.14: FE-SEM cross-sectional image of sample x=0.3 93

Figure 4.15: Y/Ho ratio dependence of critical current density (J_c) 95

List of Tables

Table 1.1: Lattice structure of different materials 17

Table 2.1: Specifications for LS-2147 Pulsed Nd:YAG Laser Deposition Machine 45

Table 3.1: Optimized PLD parameters for $(Y_{1-x}Ho_x)Ba_2Cu_3O_z$ films on 100 MgO substrates 69

Table 3.2: Particle density of $(Y_{1-x}Ho_x)Ba_2Cu_3O_z$ films 72

Table 4.1: Bridge dimensions of patterned samples 84

Table 4.2: Optimized PLD parameters for $(Y_{1-x}Ho_x)$BCO films on STO Substrates 88

Table 4.3: T_c and thickness for $(Y_{1-x}Ho_x)$BCO films on STO substrates 93

Table 4.4: I_c and J_c of $(Y_{1-x}Ho_x)$BCO films on STO substrates 94

CHAPTER 1

Introduction

1 Introduction

1.1 Background and Objectives of the Work

Since the 1986 discovery of high temperature superconductivity (HTS) in cuprate oxide superconductors [1], such as La-Sr-Cu-O (LASO), Y-Ba-Cu-O (YBCO), Bi-Sr-Ca-Cu-O (BSCCO), Tl-Ba/Sr-Ca-Cu-O (TBCCO), and Hg-Ba-Ca-Cu-O (HBCCO), extensive studies have been carried out worldwide to elucidate the mechanisms of superconductivity and to develop the applications of those HTS compounds. Great attention has been particularly paid to the research and development of superconducting thin films due to the following motivations. One is the potential of HTS thin films to give in sight into the fundamental mechanisms governing HTS [2]. The other involves the various electronic applications that high-quality thin films might enable, including low-loss microwave cavities, filters, bolometers and superconducting quantum interference devices (SQUIDS) [3]. For large current applications, HTS tapes and wires are very desirable. The first generation of superconducting tapes (1G) is based on Ag sheathed Bi-Sr-Ca-Cu-O tapes or wires fabricated using the powder-in-tube (PIT) technique. However, the BSCCO/Ag tapes and wires suffer serious degradation in critical current density in high magnetic field and have a high fabrication cost, hindering their practical application.

Later, a remarkable progress in development of electrical wire application has been achieved especially in "coated-conductor" which has a basic architecture of flexible metal (typically Ni-based alloy) tapes coated by thin film superconductor. This type of wire is also called "second generation (2G)" wire. Prototype long wires of hundreds meters with several MA/cm^2 of critical current density (J_c) have been successfully fabricated [4]. Among the many kinds of high-temperature superconductors (HTSC's) having a critical temperature (T_c) higher than liquid-

nitrogen temperature (77.3 K), $REBa_2Cu_3O_z$ (REBCO; RE: Y or rare-earth element) has been particularly selected as the most suitable material for the coated-conductor according to its excellent critical-current (I_c) performance in external magnetic field.

In coated-conductor fabrication, many kinds of deposition process have been used to prepare REBCO films. Among them, pulsed-laser-deposition (PLD) method, which is one of laser-abrasion/sputtering processes, has been extensively chosen. Especially KrF excimer laser is the popular choice among the PLD community because its short wavelength of 248 nm causes high pulse laser energy output [5].

However, some problems hindering coated-conductor application still remain to be solved scientifically, these include: reducing the fabrication cost and developing the most effective approaches to further enhance J_c in high magnetic fields. Possible solutions are, respectively for the former and the later, using a solid-state laser instead of excimer laser and introducing effective flux-pinning centers into REBCO films. There have been few reports on preparation of PLD-REBCO coated conductors [6,7] using another type of ultraviolet (UV) pulse laser, Nd:YAG (neodymium doped yttrium aluminium garnet; $Nd:Y_3Al_5O_{12}$)-type [8,9,10] which can generate 266 nm radiation when used in fourth-harmonic generation (4HG) mode. It is well known that Nd:YAG laser has some advantages over the excimer lasers such as easier operation, lower installation cost, higher safety and longer lifetime [11]. But the main disadvantage of the Nd:YAG laser is relatively low pulse energy [12]. However, owing to above-mentioned several advantages, development of new fabricaton process of "coated-conductor" using Nd:YAG laser is expected to give us a remarkable merit. To enhance J_c, introducing artificially designed pinning centers (APC's) such as nano-dots and nano-rods has been notable approach [13, 14] some of which are known to significantly enhance J_c in magnetic field parallel to c-axis of REBCO films.

In this study, some methods are proposed to solve the above-mentioned problems. REBCO ($(Y,Ho)Ba_2Cu_3O_z$) films are deposited by PLD method using an improved

Q-switched Nd:YAG laser and the results of crystallographic and morphological characterization for the obtained films are described and their critical-current performances are also shown. Based on the results, the possibility of the application of the Nd:YAG laser to the coated-conductor fabrication will be discussed. Ho was selected as the dopant because the ionic radius of Ho^{3+} is almost similar to that of Y^{3+} (in coordination number of 8; Y^{3+}: 0.1019 nm, Ho^{3+}: 0.1015 nm) [15] and therefore lattice distortion must not be occurred. It may be possible to create the pinning effect as a result of different electron potential energies in randomly distributed Y and Ho sites.

Furthermore, as a new approach for artificial pinning centers (APC) designing which is based on the idea that nano-scaled compositional randomness may act as effective pinning centers, REBCO films containing multiple rare-earth elements ($(RE,RE')Ba_2Cu_3O_z$) are prepared and characterized.

Characteristics of Nd:YAG laser, its advantages over excimer laser and process parameters of PLD are discussed in Chapter 2. In chapter 3, texture quality and surface morphology of (Y,Ho)BCO films prepared on MgO single crystal substrates are discussed. In addition to that influence of target-to-substrate distance (T-S distance; d_{TS}), laser energy density at the surface of the target and oxygen pressure on the texture quality are studied. Current characteristics of (Y,Ho)BCO films fabricated on STO single crystal substrates are discussed in chapter 4. Conclusions and future prospects are mentioned in chapter 5.

1.2 Other Thin Film Deposition Methods

1.2.1 Metal Organic Chemical Vapor Deposition (MO-CVD)

Chemical vapor deposition (CVD) techniques have a long tradition in the field of high-T_c superconductor technology. In the basic setup (Figure 1.1), most CVD processes employ evaporation sources (containing the respective precursors) located outside of the deposition chamber, with consecutive mixing of the vapors (with or without additional carrier gas) and introducing them to the (usually hot-wall) deposition chamber, where they decompose and inter-react on the substrate surface that thus form the film. Normally O_2, Ar and N_2 are used as carrier gas. The substrate is usually heated to provide the adequate reaction energy. With the aim of lowering the deposition temperature, precursor gases are additionally activated by introducing plasma near the substrate. [16]

Basically two groups of precursors:

(a) 2,2,6,6-tetramethy l-3,5-heptanedionates (thd)

(b) dipivalomethanates (dpm),

are used, each with their respective metal component composition Y(thd/dpm), Ba(thd/dpm)2, and Cu(thd/dpm)3. Amount of metal-organic vapor transported to the substrate depends on the rate of carrier gas flow and bubbler temperature. The oxygen can be supplied either via the carrier gas or during the post-annealing. O_2 annealing is applied after deposition temperature increases up to 800-850°C in order to crystallize YBCO. [17]

Advantages

- Films are homogeneous (composition and thickness) over large areas or batch loads as a result of the good "throwing power" and high deposition rates.

Disadvantages

- Difficult to achieve exact stoichiometry.
- Toxic waste products.

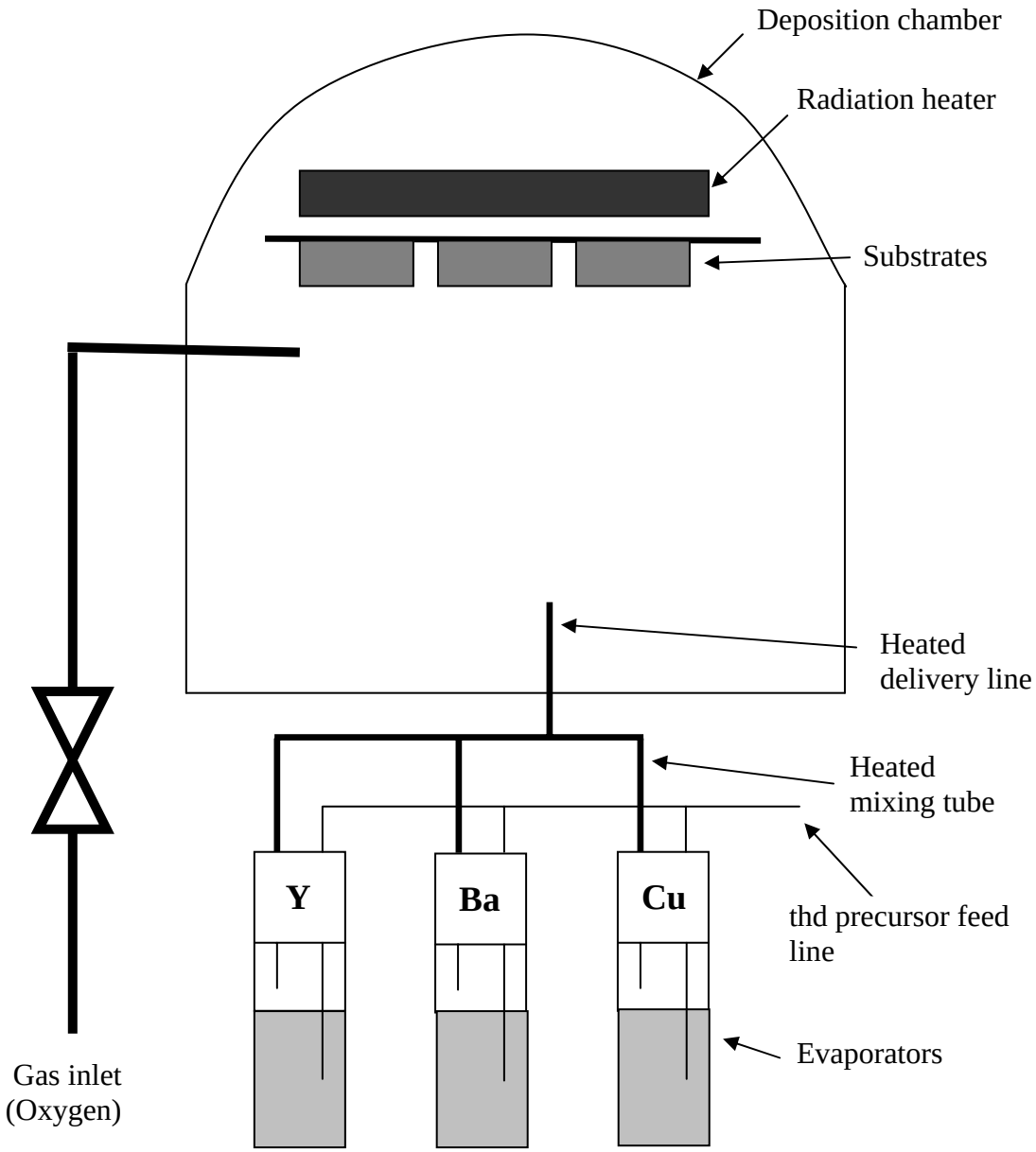

Figure 1.1: Principle of MO-CVD process.

1.2.2 Metal Organic Deposition using Trifluoroacetates (TFA-MOD)

The MOD process using a precursor solution containing metal trifluoroacetates (TFA) is an attractive candidate for YBCO thin film deposition. TFA precursor solution for fabrication of YBCO is prepared by dissolving the TFA salts of Y, Ba and Cu with a 1:2:3 cation ratios into sufficient methyl alcohol. The prepared coating solution is spin-coated onto the substrate and subjected heat treatments of the following two steps,

1) **Calcination -** Precursor film is decomposed to quasi- amorphous precursor film by slowly heating up to 400°C in a humid oxygen atmosphere.
2) **Annealing -** film is subsequently converted to crystalline oxide film of the tetragonal modification of YBCO by heating above 800°C, in a humid furnace atmosphere of argon with low oxygen partial pressure. The high-T_c orthorhombic phase is then obtained by slow cooling in dry oxygen between 600°C and 450°C. [18]

The overall reaction in the TFA process is proposed as follows,

$$0.5Y_2Cu_2O_5(S) + 2BaF_2(S) + 2CuO + 2H_2O(g) \rightarrow YBa_2Cu_3O_{6.5+x}(s) + 4HF(g) + \frac{x}{2}O_2(g)$$

In this reaction, water vapor pressure in the main gas stream, $P(H_2O)$, is a factor to control the supersaturation that determines the growth rate of the YBCO phase. Consequently, the epitaxial growth of the YBCO crystals in the thicker film should be strongly affected by the $P(H_2O)$. [19]

Advantages

- low cost of non-vacuum processing equipments are used
- Starting metal composition can be easily controlled.

Disadvantages

- Long pyrolysis steps are generally required.
- Highly corrosive HF gas is produced during the process.

1.2.3 Sol - Gel Method

Precursors and Gel Preparation from Acetates

Yttrium, barium and copper acetate solutions (around 200 $mM1^{-1}$) are prepared under agitation at 80°C. Ammonia or ethylene diamine are used to adjust the pH valve. The solutions were maintained at 80 °C for 16-24 h until viscous liquids were obtained due to slow evaporation. [20]

Precursors and Gel Preparation from Alkoxides

Copper ethoxide, barium isopropoxide, yttrium isopropoxide are used to make the solution. Mixture of isopropanol, acetic acid and water is used as solvent because copper ethoxide ($Cu(OC_2H_5)$) is not soluble in ordinary alcohols. This procedure results in considerable reduction in the reactivity of the alkoxide and thus allows the controlled preparation of a gel. The pH valve is adjusted during the whole reaction by addition of ammonia. This was necessary for avoiding segregation of the various constituents. The solution was maintained at 75°C for 48 h. The final gel is green and viscous. [20]

Preparation of the Film on Substrate

In most cases modified substrates are used. Alumina and YSZ were modified by

impregnation with a saturated solution of $AgNO_3$ which is subsequently evaporated by heating at 150 °C. Several layers of the gel were applied using a glass tube.

Calcination is done in two steps. The first calcination at 700 °C for 3 h produced a film with many cracks. These cracks could be eliminated by gently rubbing the surface of the film. Following this process the film is calcined again at 940°C for 1h and annealed at 475 °C for 12h in an oxygen atmosphere. [20]

1.2.4 Molecular Beam Epitaxy (MBE)

Molecular beam epitaxy is in several respects similar to the co-evaporation technique except that the deposition is carried out mostly sequentially rather than simultaneously. A distinct characteristic of MBE is the extremely low background gas (activated oxygen or ozone) pressure (10^{-3} Torr) that allows the application of reflective high-energy electron diffraction (RHEED) analysis to track film characteristics on a monolayer basis during growth. The individual components that form the film are evaporated by electron-beam or conventional resistance heating sources. [16]

In YBCO film preparation, Y, Ba and Cu are deposited separately and sequentially as thin layers and desired homogeneous composition is obtained by diffusion in a post-annealing. To facilitate a thorough inter-diffusion during annealing to form the superconducting phase, it is necessary that the film thickness for each individual component be sufficiently small, and most researchers deposit layers of a thickness between 10 nm and 240 nm at deposition rates below 0.3 nm/s [21]. Low deposition rates are essential to ensure formation of a homogeneous and defect-free film, and film thickness ratios for the individual components determine the stoichiometric composition of the film after annealing.

Advantages

- Films of precisely controllable atomic layers and without any macro particles, can be prepared by MBE. [21]
- It is an excellent research tool for investigating problems of interface formation, nucleation, and film growth phenomena. [21]

Disadvantages

- Relatively complicated system
- It is not used to prepare high thickness films because of the low deposition rate.

1.2.5 Sputter Deposition

Magnetron or ion beam sputter deposition technologies (MST/IBST) constituted one of the first approaches to depositing thin superconducting films. The principle of sputtering is based on the production of particles (neutrals, ions) that are emitted from a target as a result of collisions of high-mass gas ion (usually argon) bombardment **(**Figure 1.2**).** The argon ions are either produced in a separate ion source and directed toward the target (IBST), or a magnetron-assisted plasma is created in front of the target plate where the argon gas is ionized and these ions are directed toward the target surface by the applied magnetic field (MST). The substrate is facing the target surface in a manner that causes the emitted target particles and additional reactive gases (e.g., oxygen) to grow as a film. The reaction between gas and emitted target particles is assisted by substrate heating to ensure the formation of the desired film structure and stoichiometry**.** [16]

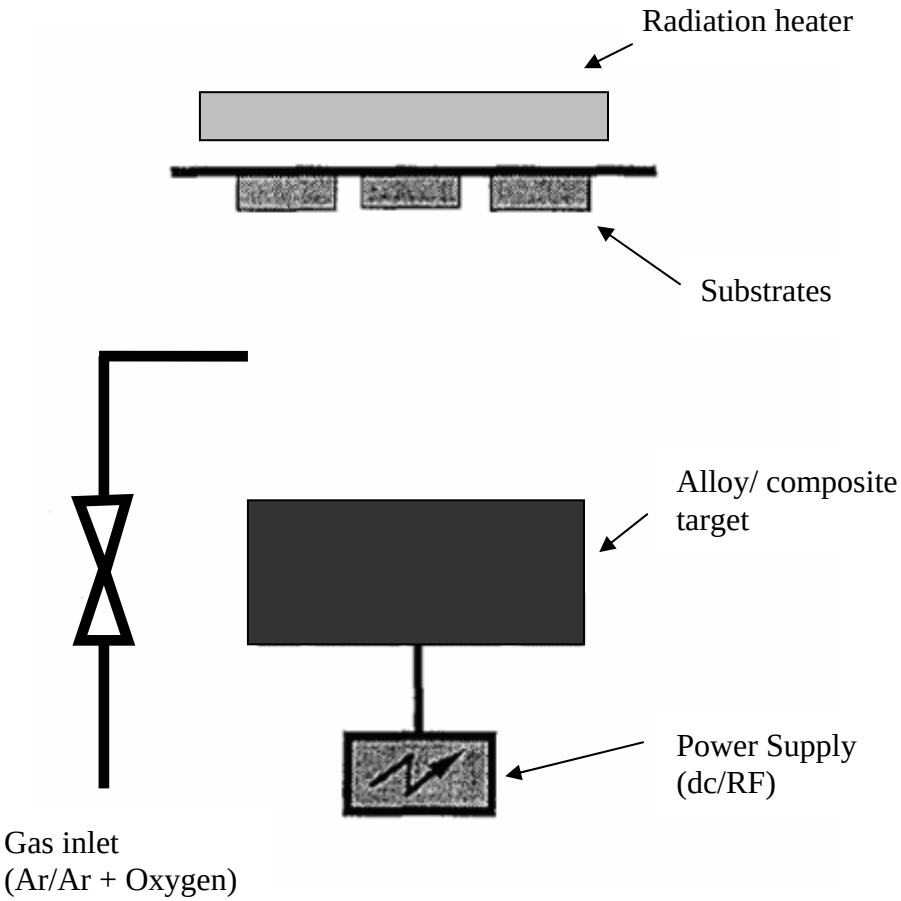

Figure 1.2: Basic Sputter Deposition**.**

The properties of the films are quite sensitive to the process parameters of MST, which are;

- Deposition mode (RF or DC)
- Gas composition (reactive/ nonreactive) [22]
- Substrate position (on axis, off-axis) [22]
- Target alignment (single/multi target) [22]
- Substrate temperature
- Gas pressure

Advantages

- Relatively easy experimental setup (Fig. 3).

Disadvantages

- In most cases the film composition does not reflect the target composition.
- When substrates face the target (on-axis) for maximum deposition rate, negative oxygen ions produced in the sputtering plasma causes backsputtering effect on the substrate that etches the growing film, depleting it of some elements (Cu, Ba) more than others. [22]

1.2.6 Co-evaporation

The basic principle of co-evaporation techniques involves the simultaneous and continuous evaporation of two or more metallic components (usually one source for each element in the film except oxygen) for the high-T_c film in an atmosphere of oxygen and/or other reactive gases. the individual elements stemming from the evaporation sources reach the substrate and form the desired structure with the help of thermal energy supplied by filament heating, but in many instances the reactivity of the gas is too low (or the necessary substrate temperature is too high), requiring additional activation by plasma **(**Figure 1.3**).** Most commonly used evaporation sources are resistance-heated or electron-beam evaporators. [16]

Usually, the evaporation rate of each source is measured in situ by quartz crystal rate monitors that are either manually or electronically looped with the power supply of the corresponding evaporation source. For Y-Ba-Cu-O films, yttrium and copper are almost always evaporated as pure elements; barium can also be evaporated as a pure element but requires careful handling due to its high affinity to oxygen, water vapor, and CO_2 when exposed to air , and therefore BaF_2 is often used as a more inert alternative. [23]

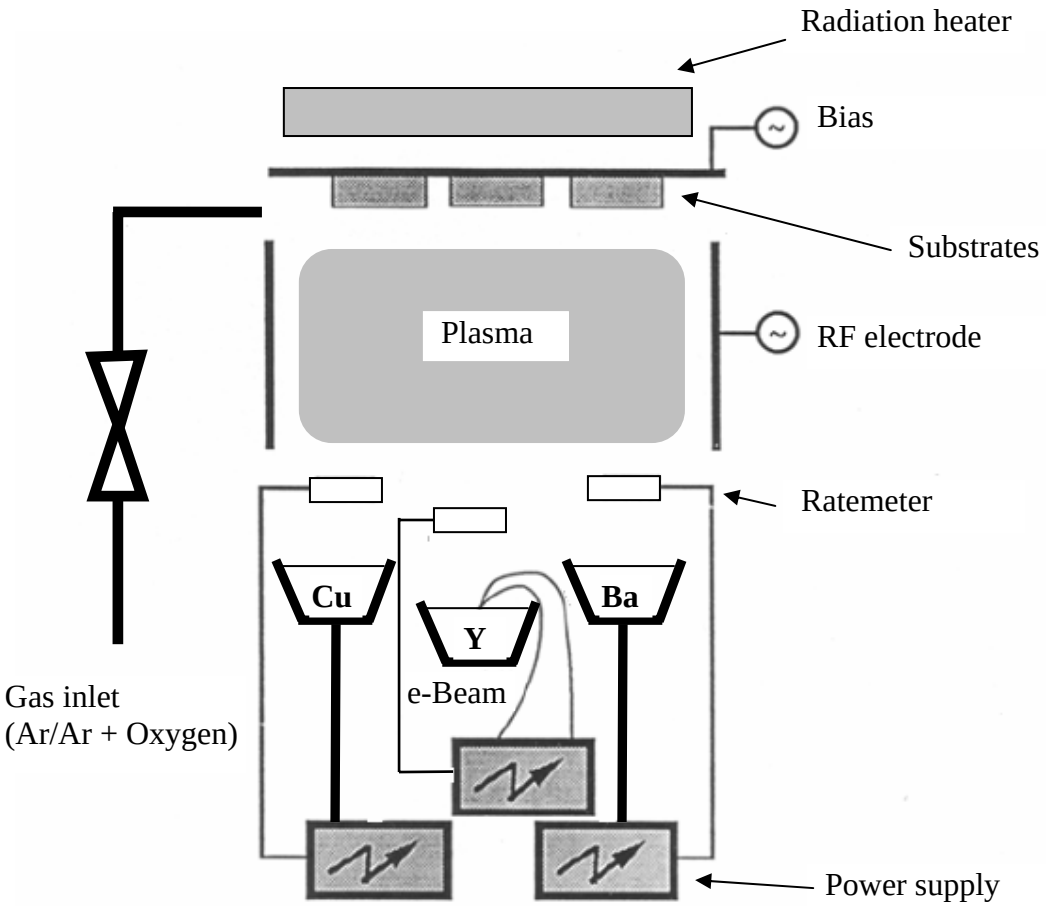

Figure 1.3: Principle of thermal co- evaporation.

Advantages

- Individual control of deposition rate of each component (Capable of keeping the stoichiometry).
- Reduced deposition temperature
- Better large-area film homogeneity

Disadvantages

- Relatively complicated system

1.3 Substrate Materials used for Thin Film Deposition

1.3.1 Substrate Requirements

For the development of a reliable deposition technology for high-quality HTS thin films, the choice of the substrate material is of primary importance. The basic requirements for the substrates can be summarized as follows.

1.3.1.1 Chemical Compatibility

One of the first issues that must be dealt with in determining the suitability of a substrate for a HTS film is the chemical compatibility of the two materials. This is true whether or not the film is epitaxial. Ideally, there should not be any chemical reactions between the film and substrate. Regardless of the specific film growth method used, the substrate must be unreactive in the oxygen-rich ambient required for growth and processing.

1.3.1.2 Crystallographic Lattice Match

It is required to have similar or nearly equal lattice parameters between the substrate and film material in order to grow the film epitaxially with maximum thickness [24]. The best HTS films grown to date, with higher critical current density, improved morphology and stability over time, are epitaxial on their substrates.

Generally two classes of substrates can be distinguished;

(a) Compatible Substrates

HTS material can be deposited without a buffer layer. Deposition onto compatible substrates is generally easier.

(b) Non Compatible Substrates

These substrates are covered by epitaxial buffer layer prior to the deposition of the HTS film owing to large lattice mismatch and/or chemical interaction between substrate and HTS material.

1.3.1.3 Similar Thermal Expansions

Large difference of thermal expansions in between the substrate and film material results in loss of adhesion or film cracking during thermal cycling.

1.3.1.4 Surface Roughness

In order to successfully deposit the buffer and superconducting layers, the surface of the substrate must be smooth and flat. Any surface irregularities on the substrate will be duplicated in the buffer and superconducting layers, resulting in degraded superconducting properties. The principal factors affecting the surface quality of the substrate have been identified as rolling damage (function of roll roughness) and grain boundary grooving during annealing [25]. The surface smoothness can be enhanced by mechanical and/or electrolytic polishing prior to deposition of the buffer and superconducting layers, although this may contaminate the surface and introduce strain into the grains.

1.3.2 Different Types of Substrates

High-temperature superconducting films have been grown successfully on many different substrates. $LaAlO_3$, $SrTiO_3$ and MgO are typical substrates used for YBCO deposition. Among these substrates, $SrTiO_3$ is extensively used because its lattice constant is almost similar to YBCO (Table 1.3) and does not react with YBCO even at relatively high temperatures. But $SrTiO_3$ is too expensive and its high-loss dielectric constant makes it unsuitable for electronic applications.

The relatively large lattice misfit (around 8%) between YBCO and MgO leads to the generation of tilt grain boundary and dislocation within YBCO films. But it can be used as substrate for YBCO because of their excellent dielectric properties: constant and low loss tangent [26].

Buffer layer provides epitaxial growth by reducing the lattice mismatch between substrate and HTS material and provides a sufficient barrier against inter-diffusion of substrate and HTS material. CeO_2 has proven to be one of the most effective buffers owing to its favorable thin-film growth characteristics, minimal chemical interaction and good lattice match with most HTS materials. One of the most ideal substrates especially for applications in the field of microwave electronics is (1102)-oriented Al_2O_3 (r-cut sapphire), which possesses high crystalline perfection and low-loss dielectric constant [24]. But it readily reacts with YBCO, therefore CeO_2 buffer layers are applied in order to provide sufficient barrier against diffusion and reduce the lattice mismatch between two materials.

Yttrium-stabilized zirconium oxide (YSZ) and CeO_2 are the best buffer layers for YBCO due to the low level of lattice mismatch with YBCO (Table). Nevertheless, buffer layers are added for a few cases of compatible substrates, e.g. CeO_2 buffer layer on $LaAlO_3$ substrates reduce the probability of *a*-axis growth [27].

Specially, the 2G wire with YBCO HTS on a RABiTS (rolling assisted bi-axially textured substrate) architecture used by American Superconductor Corporation Inc. (AMSC) is made up of three buffer layers on textured Ni-W (5%) tape. Y_2O_3 serves as a seed layer on 75 μm thick Ni-W metal substrate. Yttrium-stabilized zirconium oxide (YSZ) is deposited as a barrier layer and CeO_2 plays the role of cap layer [27].

Table 1.1: Lattice structure of different materials

Material	Lattice configuration	Lattice parameters (Å)
YBCO	Orthorhombic	a=3.89, b=3.82
YSZ	Hexagonal	a=5.14
CeO_2	Hexagonal	a=5.41
MgO	Rock-salt	a=4.213
$SrTiO_3$	Perovoskite	a=3.905
Al_2O_3	Hexagonal	a=4.777
$LaAlO_3$	Perovoskite	a=3.793

1.4 Film Nucleation and Growth

In considering the general theory of film nucleation and growth, three conventional modes of film nucleation and growth can be discussed.

- Three-dimensional island growth (Volmer-Weber).
- Two-dimensional full-mono-layer growth (Frank-van der Merwe).
- Two-dimensional growth of full-mono-layers followed by nucleation and growth of three-dimensional islands (Stranski-Krastinov).

The conventional theory of film nucleation and growth as recently reviewed by Green (1993), states that the selection of one of these growth modes by a substrate-film system depends on,

- The thermodynamics relating the surface energies (film and substrate)
- The film-substrate interface energy.

The nucleation of film-atom clusters by the vapor deposition of film atoms on a substrate involves several processes as illustrated in Figure 1.4. Film atoms arrive at a rate dependent on the deposition parameters either on bare substrate areas or on preexisting clusters of film atoms. These film-atoms can be subsequently diffuse over the substrate or clusters, attach to preexisting film-atom clusters, be re-evaporated from the substrate or from a cluster, or be detached from a cluster and remain on the substrate surface. The balance between growth and dissolution processes for a given cluster will be governed by the total free energy of the cluster, relative to an assembly of individual atoms [28].

For a cluster that is large enough to be reasonably treated as a continuum solid, this free energy can be written as,

$$\Delta G = a_1 r^2 \Gamma_{c-v} + a_2 r^2 \Gamma_{s-c} - a_2 r^2 \Gamma_{s-v} + a_3 r^3 \Delta G_v \quad \text{.....(3) [28]}$$

r	Radius of the cluster, the
Γ	Interface energy
ΔG_v	Change in volume free energy on condensation of the cluster
a	Constant that depends on the shape of the nuclei
c	Cluster
s	Substrate
v	Vapor

If, for a given cluster size, the derivative of this free-energy change with respect to atoms in the cluster is positive, then the cluster is not stable, and clusters of that size will shrink on average. If this derivative is negative, then that size cluster is stable and will grow on average.

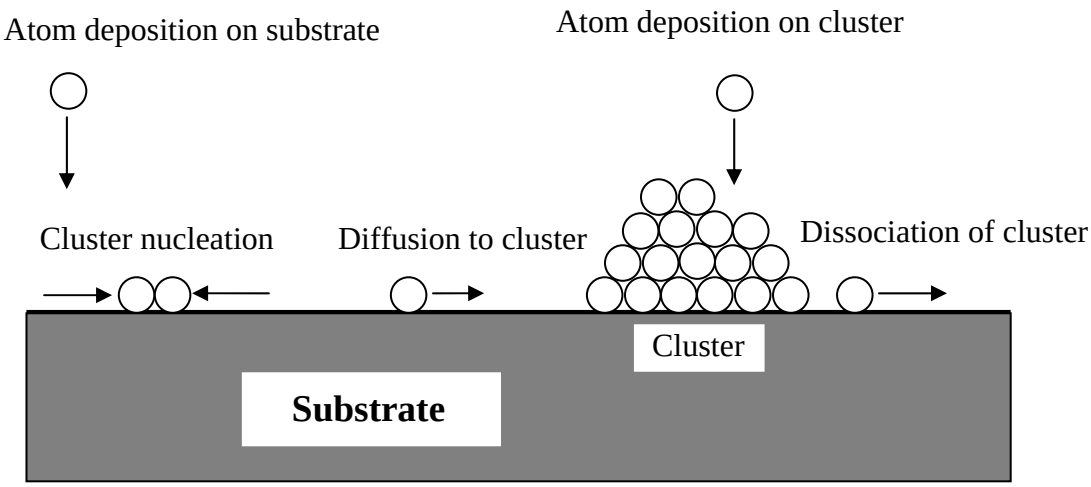

Figure 1.4: Schematic diagram of atomic processes in the nucleation of 3-D clusters.

1.4.1 Volmer-Weber Nucleation and Growth

Small clusters are nucleated directly on the substrate surface and then grow into islands of the condensed phase. This happens when the atoms (or molecules) of the deposit are more strongly bound to each other than to the substrate. A higher temperature and a lower deposition rate promote the formation of larger islands. This mode is displayed by many systems of metals growing on insulators, including many metals on alkali halides, graphite and other layer compounds such as mica. [29]

1.4.2 Frank-van der Merwe Nucleation and Growth

This mode displays the opposite characteristics. Because the atoms are more strongly bound to the substrate than to each other, the first atoms to condense form a complete monolayer on the surface, which becomes covered with a somewhat less tightly bound second layer. If the surface energy of the cluster is low and that of the substrate is high, it is energetically more favorable for the film to form as full mono-layers [30]. Full- monolayer growth still involves the nucleation and growth of

islands, but these are now only one monolayer thick, and grow to essentially complete coalescence before significant clusters are developed on the next film layer. This growth mode is observed in the case of adsorbed gases, such as several rare gases on graphite and on several metals, in some metal-metal systems, and in semiconductor growth on semiconductors [31].

1.4.3 Stranski-Krastinov Nucleation and Growth

The Stranski-Krastanov (SK) growth mode is an intermediate case between island and layer growth and occurs in a number of instances in which layer growth would be anticipated on surface energy grounds. Initial deposition leads to the formation of one, or in some instances more, strained mono-layers, whose structure is strongly influenced by the underlying substrate. Further deposition produces an adatom layer, from which three-dimensional islands eventually nucleate and grow [31]. The most obvious feature that could cause 3-D cluster nucleation over full mono-layers is increase of layer thickness in the stress due to mismatched lattice spacing [28]. The number and structure of the adsorbed layers, and the number density and shapes of the islands which form, depend on the deposition conditions and on the particular film/substrate system. In particular, the island density has been found to be a strong function of substrate temperature. There are now many examples of its occurrence in metal-metal, metal-semiconductor, gas-metal and gas-layer compound systems [30].

1.4.4 Effects of Substrate Surface Microstructure

The preceding descriptions of thin film nucleation and growth modes have implicitly assumed that nucleation occurs homogeneously at random locations on the substrate surface. In many deposition experiments, however, substrate surface defects, such as atomic steps, point defects, and dislocation intersections, provide low-energy sites at which nucleation preferentially occurs [28]. In the presence of

such heterogeneous nucleation sites, the nucleation rate and nuclei density will be controlled by the distribution of low-energy sites at low super saturations. At sufficiently high super-saturation, the homogeneous nucleation rate can overwhelm the heterogeneous rate. In principle, heterogeneous film nucleation and growth can be treated by essentially the same mathematics used for the homogeneous case simply by accounting for both low and high energy sites, but the equations become considerably more complex if the problem is treated generally. In comparing results of film nucleation experiments, the most important fact to note about heterogeneous effects is that differences in substrate preparation can dominate any differences in kinetics [31].

1.5 Pinning Improving Methods

Following the discovery of type-II high-temperature superconductor which is comprised of metallic compounds and alloys with higher T_c, work has been proceeded to develop these materials for power applications. One of the problems that researchers have faced is motion of magnetic flux lines (vortices) which yields undesirable dissipation of energy and limits the critical current density J_c [32].

In a magnetic field, B, the magnetic vortices with quantized flux ϕ_0 and spacing, $a_0 = (\phi_0 / B)^{1/2}$ experience a force, called Lorentz force, $F = I \times B$. Figure 1.5 shows that this force is perpendicular to both applied magnetic field and the direction of the current flow [33].

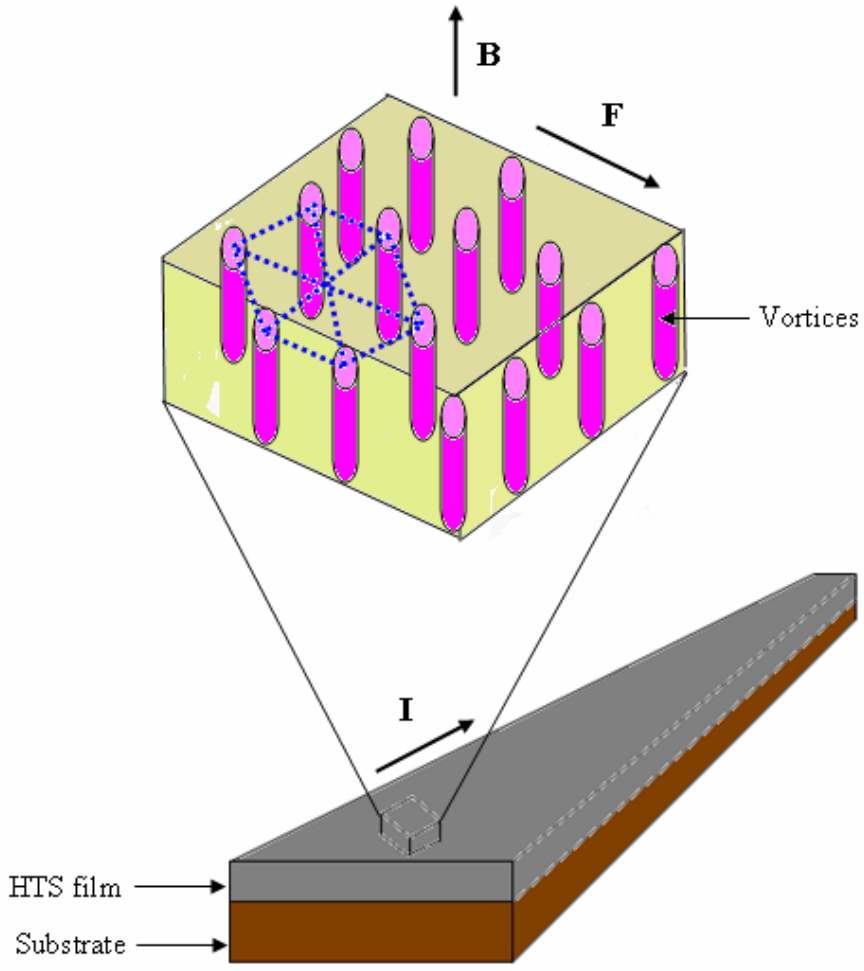

Figure 1.5: Schematic view of magnetic vortices in superconductor.

Defects or imperfections (chemical or structural) within high temperature superconductors are energetically favorable sites to pin magnetic flux-lines. This phenomenon is known as pinning effect which tends to increase the current density up to high levels. The pinning force of one individual defect depends on its size and shape, as well as on its composition and structural interaction with the matrix [34]. In general, increasing the density of pinning sites will initially increase the J_c, but beyond some optimum density performance will deteriorate [34].

In the absence of extrinsically introduced defects, the J_c of REBCO films is much higher for fields applied parallel to the *ab*-plane, *H*//*ab*, than for fields applied parallel to the *c*-axis, *H*//*c*. This anisotropy is due to the strong intrinsic pinning arising from the layered Cu-O structure [35]. Significant research has therefore been directed at improving the pining for *H*//*c*.

Basically pinning centres can be divided into two categories; Natural pinning centres and artificial pinning centres (APC). Natural pinning centres are intrinsically formed defects during the film growth such as Precipitates, Misfit dislocations, Voids, In-plane and out-of-plane misorientation. APCs are intentionally introduced into the film by various techniques and usually described as 1D (one dimensional), 2D and 3D pinning centres. Columnar defects, linear defects, nanorods and self-aligned nanoparticles introduced into REBCO (RE = Er, Gd, Nd) films prepared by PLD are known as 1D APCs [36]. Grain boundaries are considered as 2D APCs. The defects of precipitates of secondary phases or non-superconducting inclusions, randomly dispersed in the film can be referred as the 3D APCs [36].

1.5.1 Columnar Defects via Heavy-Ion Irradiation

Columnar Defects generated by heavy-ion irradiation are promising structure for pinning magnetic flux lines and enhancing critical currents in superconductors with high transition temperatures. Columnar Defects consisting of linear damage tracts with the size of 100 Å in diameter and tens of micrometers in length can be produced by heavy ion bombardment at energies on the order of several hundred mega electron volts [37]. Quantitatively, the interaction of a flux line with such a linear defect should result in a pinning energy that is much larger than what would be obtainable by use of a random array of point defects.

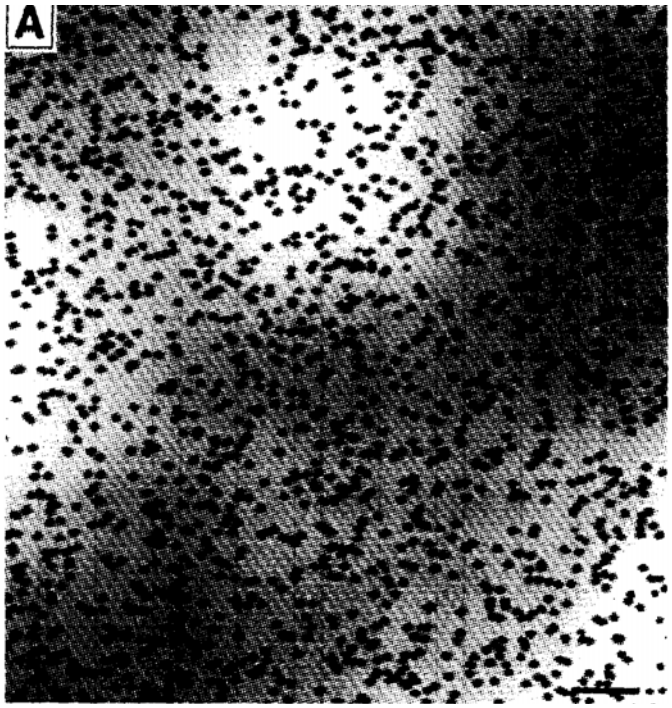

Figure 1.6: AFM images recorded on etched surfaces of BSCCO single crystals that were irradiated with 276 MeV Ag^{2+} ions to produce columnar defect densities of 1.5 x 10^7 defects per square centimeter [37].

When HTSC are irradiated with electrons, protons, neutrons and light ions with incident energies up to several MeV, defect formation is only due [38] to nuclear

energy loss. These direct collisions result in a defect formation [39] through a displacement of the primary recoil atom and, for high enough recoil energy, through collision cascades whose size increase with the primary recoil energy. For instance, around 1 MeV electron irradiation creates only point defects, while fast neutrons produce cascade defects of 50 to 100 Å in diameter [40].

As heavier and more energetic ions are considered, the electronic energy loss becomes progressively more important as compared to nuclear energy loss. For example, for Xe ions with energies in the GeV range, electronic stopping power is around 2000 times higher than nuclear stopping power. In this limit, each ion creates a cylinder of amorphized material or latent track along its path.

1.5.2 Introducing Nano-rods

$BaZrO_3$ nanorods are known to be effective pinning centers as *c*-axis-correlated pinning centers. Yttria-stabilized zirconia (YSZ) was added to the YBCO target, and $BaZrO_3$ formed by reaction [41], presumably leaving a Ba-deficient YBCO film matrix. A fascinating feature is the self-assembly of vertical arrays of $BaZrO_3$ particles known as nanorods (Figure 1.7). It is thought to arise when impurity islands preferentially nucleate in the strain field above buried impurity particles [42]. The strain is due in part to the crystalline lattice mismatch between the impurity and host material, and this is probably why 'nanorod' is observed in a high mismatch (9%) system such as YBCO/$BaZrO_3$ whereas it is not observed when the mismatch is lower (2.5%), as with Y_2O_3 nanoparticles [43].

In one variation, $BaZrO_3$ nanorods are formed inside YBCO film by means of a 'Surface Modified' YBCO target: a thin and narrow YSZ sector, which was cut from a YSZ single crystal, was stuck on the target [37]. Recently, Varanasi et al [44] have shown another method, which is to insert a 30° slice of the second phase material into the main YBCO target to yield a 'Pie-shaped' target. In this method, the

$BaSnO_3$ dopant phase can be ablated in a periodic fashion yielding c-axis correlated nanorods finely dispersed throughout the entire film thickness.

The density of $BaZrO_3$ nanorods in YBCO films can be controlled by varying the $BaZrO_3$ content in a target. The $BaZrO_3$ addition has two functions for superconductivity; one is the improvement of pinning forces due to the addition of pinning centers and the other is T_c degradation.[45] Furthermore, the length of $BaZrO_3$ nanorods is found to be controlled using two types of target: pure YBCO and a mixture of YBCO and $BaZrO_3$. Varying the $BaZrO_3$ nanorod length has an effect on the pinning mechanism [45]. In particular, magnetic field angle dependences of J_c are varied from *c*-axis-correlated pinning to nearly random pinning by changing the nanorod length. The magnetic field at the crossover of the pinning mechanism seems to be adjusted by the $BaZrO_3$ nanorod length. [45].

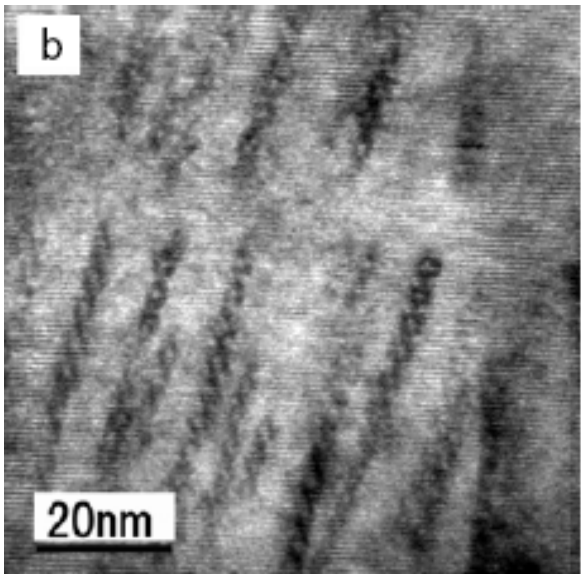

Figure 1.7: Magnified cross-sectional TEM image of YBCO film with $BaZrO_3$ nanorods [45].

1.5.3 Introducing Second Phase Nano-particles

Various materials such as Y_2O_3, Y_2BaCuO_5 (Y211), $BaZrO_3$, $BaIrO_3$, Nd_2O_3 etc [46-48] in pulsed laser ablated (PLD) YBCO films have been recently investigated for creating nanoparticles for flux pinning. The pinning effect of each of these materials and processes provides effective pinning at various magnetic field levels.

1.5.3.1 Addition of Y2BaCuO5 (Y211) Nanoparticles

Second phase Y211 particles of nanometre size are introduced by growth of alternating multilayers of ultrathin Y211 and Y123 using separate Y123 and Y211 composition targets. Microscopy studies (Figure 1.8) reveal a near-uniform dispersion of second phase Y211 nanoparticles grown by the island-growth mode in YBCO. [49]

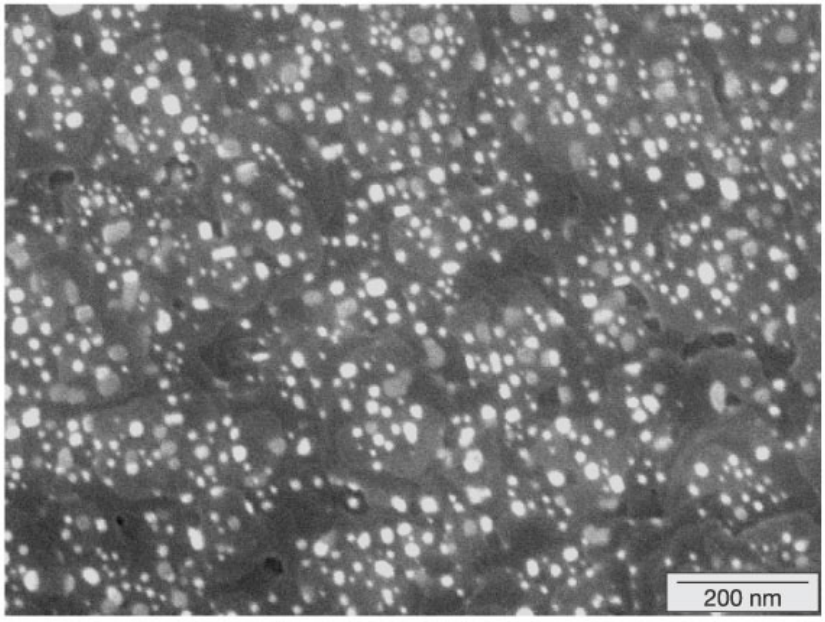

Figure 1.8: SEM image of (Y211 $\sim_{1.1\ nm}$/Y123 $\sim_{12.6\ nm}$) $\times$ 25 multilayer film. White-image nanoparticles have average particle size 14.8$\pm$0.7 nm and areal number density $\sim 1.1 \times 10^{11}$ particles cm^{-2} [49].

1.5.3.2 Y_2O_3 Doped YBCO Films by Surface Modified Targets

Nanoparticles of Y_2O_3 doped YBCO films are produced using surface modified targets: a thin (0.5 mm) and narrow (its area is about 2.5% of the surface area of the YBCO target) Y_2O_3 sector, which was cut from a Y_2O_3 single crystal, was stuck on the target [36].

Another way to introduce second phase particles in PLD YBCO films is by the use of a doped YBCO target. YBCO powder is blended with a desired amount of second phase materials and sintered together to form a composite target of superconductor and pinning material [39]. However, reactions with the pinning material and YBCO during the target preparation are possible in this approach if the pinning material is not chemically compatible with the YBCO [50].

1.5.4 Substrate Surface Decoration

Surface decoration, the earliest method used, has been accomplished by depositing metal (Ag, ref. 51; Ir, ref.52) or oxide (Y_2O_3, ref.53) nanoparticles on the substrate before YBCO film growth, or by processing an oxide layer (CeO_2, ref. 54; $SrTiO_3$, ref. 55**)** in such a way that nanoscale outgrowths develop naturally on the deposition surface. The particles, ranging in size from 10–100 nm, produce a disruption in the YBCO that can enhance flux pinning. There is, however, no clear and consistent picture regarding the nature of the disruption and the effect on performance. The most likely scenario is that the YBCO lattice planes are buckled or distorted above the nanoparticles, resulting in low-angle grain boundaries or
dislocations that may thread to the substrate surface.

In one case Y_2O_3 surface particles produced *c*-axis-correlated defects, with the expected enhancement of J_c when the field is parallel to these defects [56]. In contrast, J_c enhancement that appears as random pinning has been produced with iridium surface particles, but random pinning is typically associated with a homogeneous distribution of point defects distributed throughout the film volume,

and not the planar distribution here. It has been reported [47] that buckling of the YBCO planes above the particles, and the films are thin (100–200 nm); perhaps strain fields present through the full thickness are creating the appearance of a volumetric particle distribution.

1.5.5 Low-Temperature Growth Process for $Sm_{1+x}Ba_{2-x}Cu_3O_{7-\delta}$ Films

Low-temperature growth (LTG) process is proposed for fabrication of the non-stoichiometric composition of $Sm_{1+x}Ba_{2-x}Cu_3O_{7-\delta}$ ($x \leq 0.12$) films with improved J_c [57]. This process involves the following procedure. First, SmBCO seed layer with an approximate film thickness of 100 nm is deposited on an MgO substrate at a high growth temperature (T_s= 830°C). Then, SmBCO upper layer with a thickness of 500–600 nm is deposited at a low T_s (740°C) [57].

In the upper layer, which was fabricated at a low T_s, compositional changes occurred both in directions parallel and perpendicular to the surface of the substrate. Thus, it appears that the interior of the LTG-SmBCO thin film contains diffused clusters of a three-dimensional Sm-rich phase (Figure 1.9). It is thought that such a Sm-rich phase operates as a magnetic field-induced pinning center.

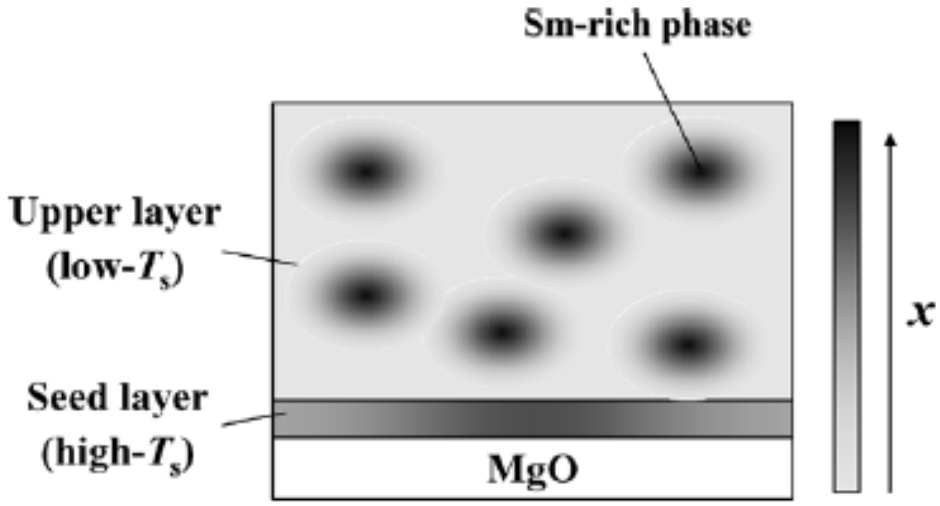

Figure 1.9: Schematic drawing of the LTG-SmBCO thin film inferred from microstructural observations based on the TEM-EDX analysis [57].

1.5.6 Replacement of Y with Other RE Elements

The most complex and poorly understood pinning enhancement mechanisms arise from replacement of yttrium in YBCO films with RE elements. Although it has long been known that such REBCO compounds show different and sometimes enhanced field-dependent J_c behaviour compared with YBCO, the reasons for this are uncertain. However, obvious influences are the increased transition temperature (T_c) values [58], and growth thermodynamics and kinetics that are thought to yield improved film microstructures [59].

Previous studies reveal that $GdBa_2Cu_3O_{7-\delta}$ shows significant in-field enhancement over YBCO, perhaps due to an increased density of stacking faults [60]. Promising levels of enhancement have also been reported for EuBCO [61] and SmBCO [62], although these compositions must be deposited at higher temperature [63] and oxygen pressure to control the amount of RE–Ba exchange and to achieve the required crystallinity in compounds with higher melting temperatures. Such

modifications are not needed in the heavier rare-earth elements, which are less prone to exchange with Ba and have lower melting points [64].

1.6 References

(1) A. Ibi, H. Fukushima, R. Kuriki, S. Miyata, K. Takahashi, H. Kobayashi, M. Konishi, T. Watanabe, Y. Yamada, Y. Shiohara, Physica C 525, 445–448 (2006).

(2) K. Nakaoka, J. Matsuda, M. Yoshizumi, T. Goto, Y. Yamada, T. Izumi, Y. Shiohara, Physica C 615, 463–465 (2007).

(3) V.F. Solovyov, H.J. Wiesmann, M. Suenaga, *Physica* C 14, 353 (2001).

(4) J. M. Phillips, D. Shi, High-Temperature Superconducting Materials Science and Engineering, Pergamon, Oxford (1994).

(5) N. Michael, R. Ashfold, F. Claeyssens, M. Gareth, J. Simon, Chem. Soc. Rev. 33**,** 23 – 31 (2004).

(6) T. Kusumori, H. Muto, Physica C 57-61, 337 (2000).

(7) T. Kusumori, H. Muto, Physica C 282-287, 577-578 (1997).

(8) H. C. Lee, Y.P. Kim, Optics & Laser Technology 40, 901-905, (2008).

(9) W. Zendzian, J.K. Jabczynski, J. Kwiatkowski, Optics & Laser Technology 40, 441-444, (2008).

(10) Y.F. Chen, Y.P. Lan, Appl. Phys. B 79, 29–31 (2004).

(11) D. Basting, G. Marowsky, Excimer Laser Technology, Springer Berlin Heidelberg, Germany, 385-397 (2005).

(12) W. Zendzian, J.K. Jabczynski, J. Kwiatkowski, Optics & Laser Technology 40, 441-444, (2008).

(13) S. H. Wee, A. Goyal, J. Li, Y. L. Zuev, S. Cook, L. Heatherly, Supercond. Sci. Technol. 20, 789–793 (2007).

(14) M. Murakami, N. Sakai, T. Higuchi, S. Yoo, Supercond. Sci. Technol. 9, 1015 (1996).

(15) R. D. Shannon, Acta Cryst. A32, 751 (1976).

(16) C.H. Stoessel, R.F. Bunshah, S. Prakash, H.R. Fetterman, Journal of Superconductivity 6, No.1 (1993).

(17) J. Zhao, D.W. Noh, C. Chern, Y.Q. Li, P. Norris, B. Gallois, B. Kear, Appl. Phys. Lett. 56, 2342 (1990).

(18) P. Benzi, E. Bottizzo, C. Demaria, N. Rizzi, J. Chem. Sci. 119, 631–635 (2007).

(19) T. Honjo, Y. Nakamura, R. Teranishi, H. Fuji, J. Shibata, T. Izumi, Y. Shiohara , IEEE Trans. Appl. Supercond. 13, 2516-2529 (2003).

(20) L.F. Admaiai, P. Grange, B. Delmon, M. Cassart, J.P. Issi, J. Mater. Sci. 29, 5817-5825 (1994).

(21) H.S. Wang, D. Eissler, Y. Kershaw, W. Dietsche, A. Fischer, K. Ploog, Appl. Phys. Lett. 60, 778 (1992).

(22) D. Zhang, D.V. Plant, H.R. Fetterman, K. Chou, S. Prakash, C.V. Deshprandey, R.F. Bunshah, Appl. Phys. Lett. 58, 1560 (1991).

(23) O. Nakamura, E.E. Fullerton, J. Guimpel, I.K. Schuller, Appl. Phys. Lett. 60, 120 (1992).

(24) R. Wordenweber, Supercond. Sci. Technol.12, R86–R102 (1999).

(25) T. Horide, K. Matsumoto, K. Osamura, A. Ichinose, M. Mukaida, Y. Yoshida, S. Horii, Physica C 412–414, 1291–1295 (2004).

(26) M. Ohmukai, T.Fujita, T.Ohno, Brazilian J. Phys. 31,1,(2001).

(27) K. Kim, M. Paranthaman, D.P. Norton, T.Aytug, C.Cantom, A.A. Gapud, A. Goyal, D.K.Christen, Supercond. Sci. Technol. 19, R23–R29 (2006).

(28) S.H. Seo, J.S. Song, M.H. Oh, J.S Park, Y.Z Wang, Thin Solid Films, 469-470, 149-153 (2004).

(29) J.A. Venables, G.D. Spiller, M.Hanbuck, Rep. Prog. Phys.47, 399-459 (1984).

(30) D.J. Kenny, R.E. Palmer, Surface Science 447, 126-132 (2000).

(31) E. Gillet, B. Gruzza, Surface Science, 97, 553-563 (1980).

(32) J. Gutierrez, A. Llordes, J. Gazquez, M. Gibert, N. Roma, S. Ricart, A. Pomar, F. Sandiumenge, N. Mestres, T. Puig, X. Obradors: Nat. Mater. **6,** 367 (2007).

(33) D. Christen, Nature Materials 3, 421 - 422 (2004)

(34) S.R. Foltyn, L. Civale, J.L. MacManus-Driscoll, Q.X. Jia, B. Maiorov, H. Wang, M. Maley, Nature Materials **6**, 631 - 642 (2007)

(35) A. Goyal, S. Kang, K.J. Leonard, P.M. Martin, A.A. Gapud, M. Varela, M. Paranthaman, A.O. Ijaduola, E.D. Specht, J.R. Thomson, D.K. Christen, S.J. Pennycook, F.A. List, Supercond. Sci. Technol. 18, 1533 (2005).

(36) P. Mele, K. Matsumoto, T. Horide, A Ichinose, M Mukaida, Y. Yoshida, S Hori, R Kita, Supercond. Sci. Technol. 21, 015019 (2008).

(37) Y.Zhu, Z.X. Car, R.C. Bhdhani, M. Suenaga, D.O. Welch, Phys.Rev. B, 48, 6436 (1993).

(38) H. Dai, S. Yoon, J.Liu, R.C. Budhani, C.M.Lieber, Science, 265, 1552-1555 (1995).

(39) G.P. Summers, E.A. Burke, D.B. Chrisey, M. Nastasi, J.R. Tesmer, Appl. Phys. Lett. 55, 1469 (1989).

(40) M.A. Kirk, H.W. Weber, Studies of High-Temperature Superconductors, vol 10 Nova Science, New York (1992).

(41) Y. Yamada, et al. Appl. Phys. Lett. 87, 132502 (2005).

(42) V.A. Shchukin, D. Bimberg, Rev. Mod. Phys. 71, 1125–1171 (1999).

(43) H. Wang, et al. J. Appl. Phys. 100, 053904 (2006).

(44) C.V. Varanasi, P.N. Barnes, J. Burke, L. Brunke, I. Maartense, et al. Supercond. Sci. Technol. 19, L37 (2006).

(45) A. Ichinose, K. Naoe, T. Horide, K. Matsumoto, R. Kita, M. Mukaida, Supercond. Sci. Technol. 20, 1144–1150 (2007)

(46) J.L. MacManus-Driscoll, S.R. Foltyn, Q.X. Jia, H. Wang, A. Serquis, L. Civale, B. Maiorov, M.E. Hawley, M.P. Maley, D.E. Peterson, Nat. Mater. 3**,** 439–41(2004).

(47) T.A. Campbell, T.J. Haugan, I. Maartense, J. Murphy, L. Brunke, P. Barnes, Physica C 423 (2005).

(48) J. Hanisch, C. Cai, R. Huhne, L. Schultz, B. Holzapfel, Appl. Phys. Lett. 86 122508 (2005).

(49) T.J. Haugan, P.N. Barnes, R.Wheeler, F. Meisenkothen, M. Sumption, Nature 430 (867–70) 2004.

(50) S. Kang et al Science 311, 1911(2006).

(51) A.Crisan, S.Fujiwara, J.C. Nie, A. Sundaresan, H. Ihara, Appl. Phys. Lett. 79, 4547–4549 (2001).

(52) T. Aytug, et al. J. Appl. Phys. 98, 114309 (2005).

(53) K. Matsumoto et al. Physica C 412–414, 1267–1271 (2004).

(54) J.C. Nie, et al. Supercond. Sci. Technol. 17, 845–852 (2004).

(55) B. Maiorov, et al. Supercond. Sci. Technol. 19, 891–895 (2006).

(56) P. Mele, K. Matsumoto, T. Horide, O. Miura, A. Ichinose, M. Mukaida, Y. Yoshida, S. Horii, Supercond. Sci. Technol. 19, 845–852 (2006).

(57) Y.Yoshida, et al. Jpn. J. Appl. Phys. 44, L129–L132 (2005).

(58) J.G. Lin, et al. Phys. Rev. B 51, 12900–12903 (1995).

(59) C. Kwon, et al. Phil. Mag. B 80, 45–51 (2000).

(60) Y.Yamada, et al. Appl. Phys. Lett. 87,132502 (2005).

(61) Q.X. Jia, et al. IEEE Trans. Appl. Supercond. 15, 2723–2726 (2005).

(62) C. Kwon, et al. IEEE Trans. Appl. Supercond. 9, 1575–1578 (1999).

(63) B. Stauble-Pumpin, et al. Phys. Rev. B 52, 7604–7628 (1995).

(64) J.L. MacManus-Driscoll, J.A. Alonso, P.C. Wang, T.H. Geballe, J.C. Bravman, Physica C 232, 288–308 (1994).

CHAPTER 2

Nd:YAG Laser and

Pulsed Laser Deposition

2 Nd:YAG Laser and Pulsed Laser Deposition

2.1 Nd:YAG Laser

Nd:YAG (neodymium-doped yttrium aluminium garnet; Nd:$Y_3Al_5O_{12}$) is a crystal that is used as a lasing medium for solid-state lasers. The dopant, triply ionized neodymium, replaces yttrium in the crystal structure of the yttrium aluminium garnet without strongly affecting the lattice structure, because these ions have a similar size. Generally the crystalline host is doped with around 1% neodymium by weight.

2.1.1 Theory of Operation

Nd:YAG lasers are optically pumped using a flashlamp or laser diodes. Flashlamp is an electric glow discharge lamp designed to produce extremely intense, incoherent, full-spectrum white light for very short durations. The lamp comprises a hermetically sealed tube, often made of fused quartz, which is filled with a noble gas, usually xenon, and electrodes to carry electrical current to the gas. Additionally, a high voltage power source is necessary to energize the gas. A charged capacitor is usually used for this purpose so as to allow very speedy delivery of very high electrical current when the lamp is triggered. A laser diode is a laser where the active medium is a semiconductor similar to that found in a light-emitting diode. The most common and practical type of laser diode is formed from a p-n junction and powered by injected electric current. Gallium arsenide, indium phosphide, gallium antimonide, and gallium nitride are all examples of compound semiconductor materials that can be used to create junction diodes. [1]

Nd:YAG lasers operate in both pulsed and continuous mode [2]. Pulsed Nd:YAG lasers are typically operated in the so called Q-switching mode: An optical switch is inserted in the laser cavity waiting for a maximum population inversion in the neodymium ions before it opens. Then the light wave can run through the cavity,

depopulating the excited laser medium at maximum population inversion. In this Q-switched mode output powers of 20 megawatts and pulse durations of less than 10 nanoseconds are achieved.The high-intensity pulses may be efficiently frequency doubled to generate laser light at 532 nm, or higher harmonics at 355 and 266 nm [3].

There are two main types of Q-switching:

Active Q-switching

Here, the Q-switch is an externally-controlled variable attenuator. This may be a mechanical device such as a shutter, chopper wheel or spinning mirror placed inside the cavity. The reduction of losses is triggered by an external event, typically an electrical signal. The pulse repetition rate can therefore be externally controlled. [4]

Passive Q-switching

In this case, the Q-switch is a saturable absorber, a material whose transmission increases when the intensity of light exceeds some threshold. The material may be an ion-doped crystal like Cr:YAG, which is used for Q-switching of Nd:YAG lasers. Initially, the loss of the absorber is high, but still low enough to permit some lasing once a large amount of energy is stored in the gain medium. As the laser power increases, it saturates the absorber, i.e., rapidly reduces the resonator loss, so that the power can increase even faster. Ideally, this brings the absorber into a state with low losses to allow efficient extraction of the stored energy by the laser pulse. [4]

2.1.2 Advantages of Nd:YAG Lasers

Basically two types of lasers, excimer and Nd:YAG laser, are frequently used in pulsed laser deposition method. The reflectivity of most materials is much lower at short wavelengths than at long infrared wavelengths [5]. When reflectivity decreases, very fine layers of the target surface can be removed without remarkable heating or

changing of the remainders because the penetration depth into the target is correspondingly reduced [6]. Therefore the high quality films have been prepared mostly using an excimer lasers. Especially KrF excimer laser is the popular choice among the PLD community because its short wavelength of 248 nm causes high pulse laser energy output [7].

However, Nd: YAG laser system was used in this study because it has some advantages over the excimer laser system. The life time of the Nd:YAG system normally depends on the laser pumping source (either a flash lamp or laser diode). In the case of excimer lasers, the gas fills have a short lifetime due to slow consumption of the halogen component by impurities arising mainly from degradation of the discharge electrodes and perionization pins. This process generates dust particles comprised of halogen salts. Adequate removal of these dust particles is essential for maximum gas lifetime and long optics cleaning intervals [8]. Therefore The static gas lifetime (period of time taken to drop the specified energy of laser to 50% when it is used infrequently up to 30 minutes per day) of the excimer laser system is very short relative to the Nd:YAG system. A typical value for Krypton Fluoride in an EX50 laser is 12 weeks [9].

Nd:YAG lasers typically emit light with a wavelength of 1064 nm in the infrared [10]. Starting with that wavelength, outputs at 532, 355 and 266nm can be generated by using non-linear optical crystals: Potassium Titanium Oxide Phosphate (KTP), Potassium Dihydrogen Phosphate (KDP) and Beta Barium Borate (BBO) respectively [11]. However in the case of excimer laser the gas mixture should be changed in order to obtain different energy levels; therefore it is not a convenient system. On the other hand Nd:YAG system is comparatively safe and inexpensive. Nd:YAG laser system could be a efficient and cost effective technique for production of coated conductors because it is convenient and inexpensive.

Pulsed Nd:YAG lasers are typically operated in the Q-switching mode, which leads to lower pulse repetition rates, higher pulse energies and longer pulse durations

than in excimer lasers [12]. Diode-pumped Nd: YAG lasers have the advantages of compactness and efficiency over other types [13].

2.1.3 Model LS-2147 Pulsed Nd:YAG Laser Deposition Machine

The laser operating process is based on the stimulated photon emission from upper laser level of Nd^{+3} in YAG crystal excited by a pulsed pump (flash) lamp. The Q-switch mode of operation is provided by an electro-optic KDP pockels cell. The SH generation is obtained with the non-linear KTP crystal cut for the type II phase matching. KDP and BBO crystals set in the temperature controlled ovens are used for TH and FH generaion. Heraeus noble light lamp illuminates two Nd:YAG laser rods and produces the necessary inversion of the energy level population of Nd^{+3}. The lamp and active element (AE) are set in diffuse reflector, which provides the homogeneous illumination of both AE and the filtration of UV part of pumping light.

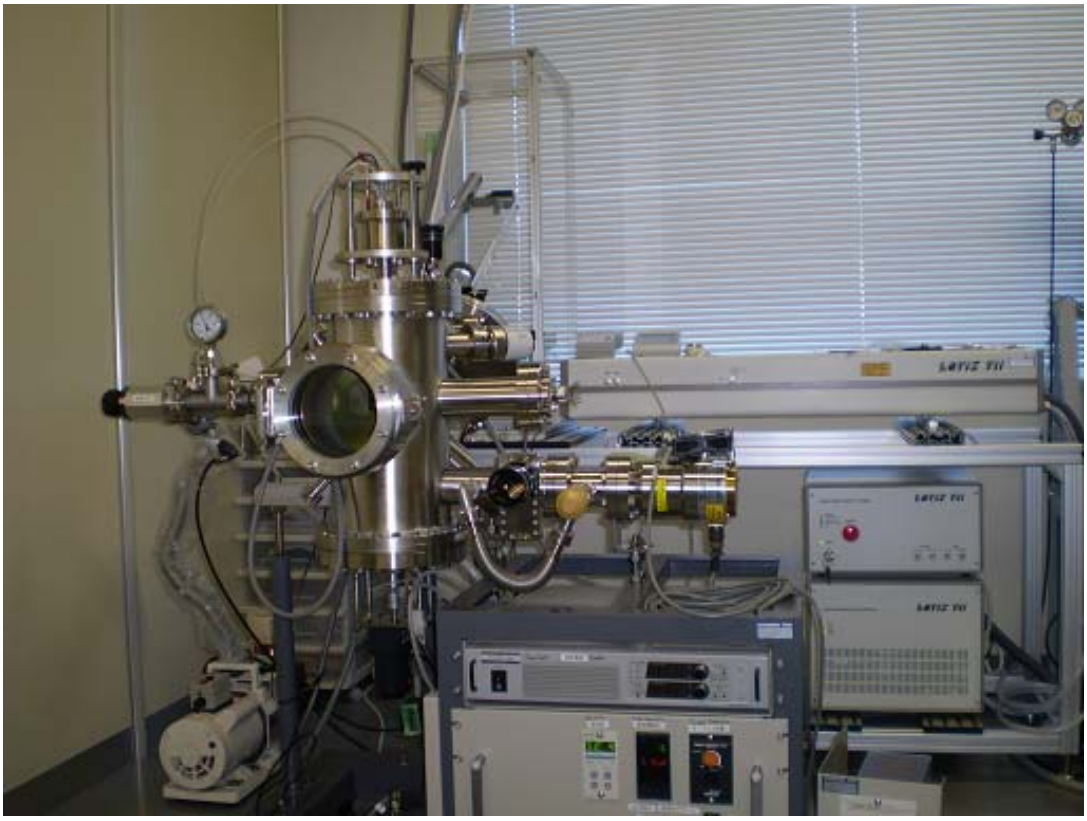

Figure 2.1: Model LS-2147 pulsed Nd:YAG laser deposition machine.

Laser Head (LH)

Laser head is one of the Key parts of the laser, which provides the conversion of electrical pump energy into laser radiation. In the LS-2147 PLD machine LH is mounted in laser emitter (LE). The triggering circuit and control plate of Q- switch is also set there. This arrangement of LE permits to eliminate high voltage connectors between LE and power supply (PS) and to increase laser safety and simplify laser construction. The base of LS-2147, LH is special double rod laser pump chamber, which allows to work oscillator-amplifier with one power supply and one cooling system [14].

Laser Cavity

The main parts of the laser cavity are trihedral corner cube prism (Figure 2.2- (5)), rear (1) and output mirrors (8). Q-switched mode is provided by the pockels cells (3) and thin film polarizer (6). Rotator is used for rotating polarization plane after passing the laser radiation across the prism (5).The intracavity mode-controlling telescope (2) fulfils two functions [14].

- Compensation of thermal lensing of AE, which is approximately a linear function of average input power to the flash lamp.
- Limit the irreducible mode content of the beam

Removable telescope (11) is used for increasing output energy and compensation thermal lens of amplifier rod.

Fundamental Frequency (FF) and SH Laser Generation

After amplification, the radiation of FF is converted to the light of SH by the KTP crystal (13) cut according to type II phase matching. The angle between the

polarization of FF and SH radiation is 45^0. The desired plane of polarization of FF and SH radiation is achieved by the rotator (10) made of the quartz crystal [14].

TH Generation

As shown in Figure 2.2, when mirror (14) is in the position (II) the pump radiation (FF and SH) falls onto non-linear crystal KDP. Since the crystal is cut for type II phase matching the polarization of the FF pump radiation is vertical (e) and the polarization of the SH is horizontal. The radiation of the TH (355 nm) is separated from the FF and SH laser by the wavelength separator (WS) and it reflects only TH laser [14].

FH generation

When mirror (14) and mirror (15) is in the position (I) and (II) respectively, pump radiation of the SH is directed to the BBO crystal (20) which is cut according to the type I phase matching, it converts SH radiation into FH light with “s” polarization. The radiation of the FH is separated from the SH light by the WS (16) shown in Figure 2.2. [14]

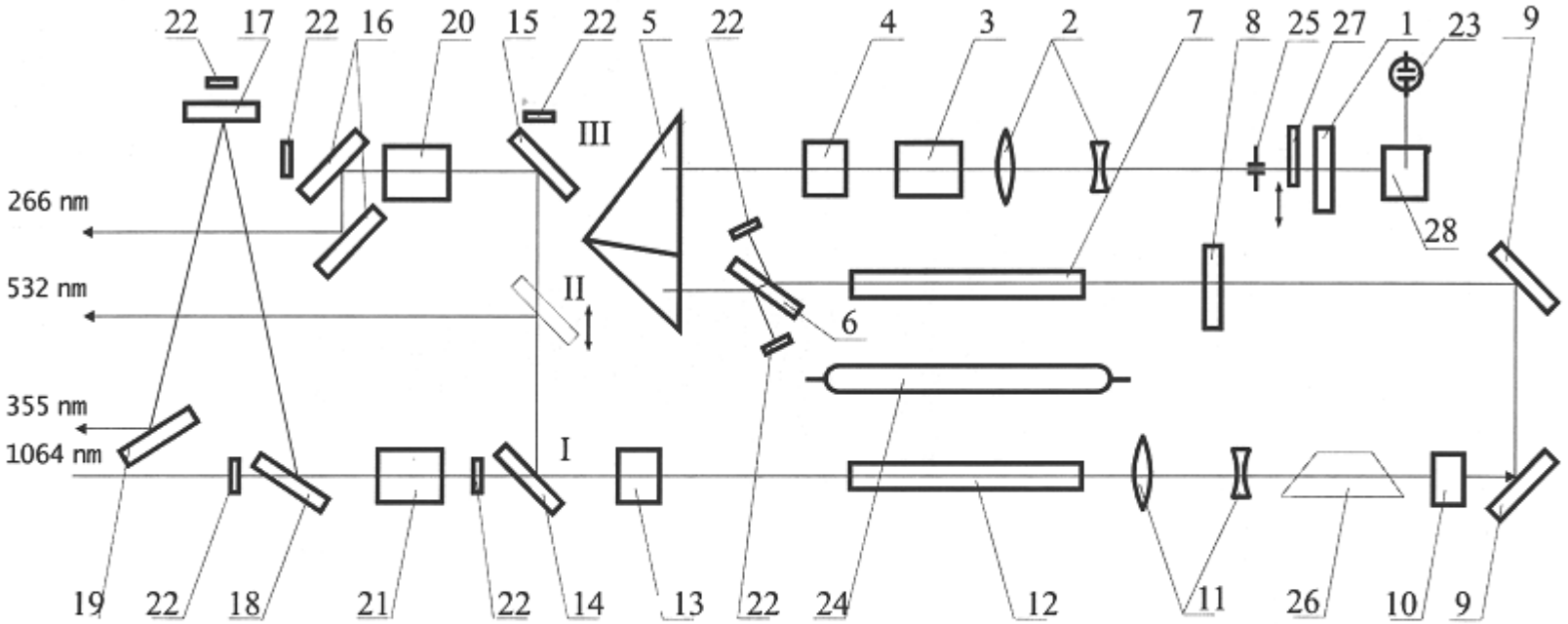

1 - rear mirror R>99.9% (1064nm); **2** - intracavity telescope; **3** - Pockels cell; **4** - rotator; **5** - corner cube prism;
6 - polarizer; **7** - AE of the oscillator; **8** - output mirror; **9** - turning mirrors; **10** - rotator 45°; **11** - telescope;
12 - AE of the amplifier; **13** - SH crystal (KTP); **14** - **19** - WS; **20** - FH crystal; **21** - TH crystal; **22** - absorption filters;
23 - light detector; **24** - flash lamp; **25** - intracavity pinhole; **26** - Dove prism (removable); **27** - shutter;
28 - right angle prism.

Figure 2.2: Optical diagram of the laser cavity [14]

Table 2.1: Specifications for LS-2147 Pulsed Nd:YAG Laser Deposition machine [14]

Parameter	Guaranteed valve
Pulse Energy (mJ), FF	850
SH	480
TH	180
FH	120
Pulse Repetition Rate (f), Hz	1; 2; 5; 10
Pulse Duration (FWHM),ns	10-18
Beam Divergency, mrad	≤ 0.7
Beam Diameter, mm	≤ 8
Pump Energy (Ep), J	≤ 65
Power Consumption, W	≤1000
Input Power Requirements	220 V, 50 Hz Single phase, 10A

2.2 Pulsed Laser Deposition (PLD) Process

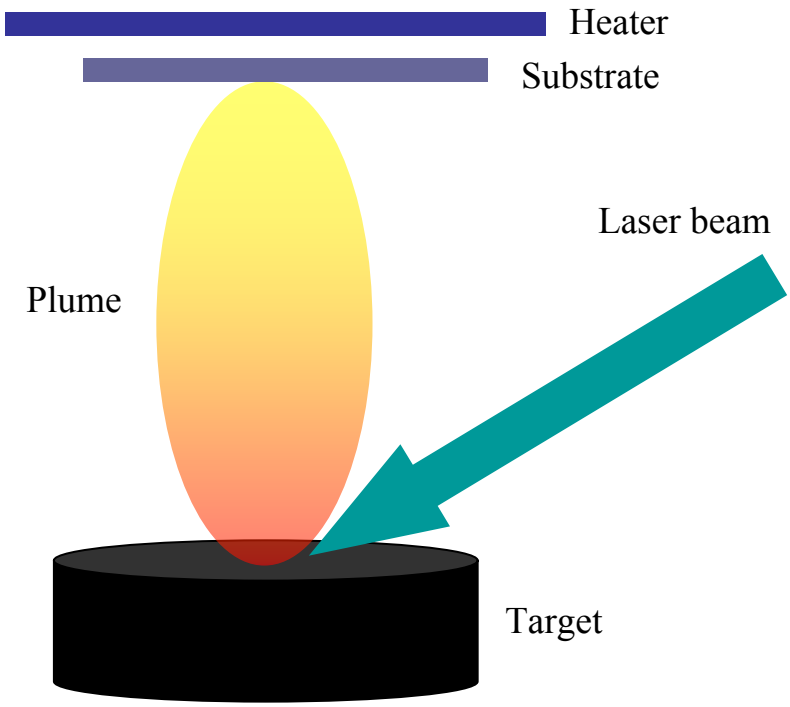

Figure 2.3: Principle of pulsed laser deposition.

Laser ablation is a materials-processing technique that has been known since the invention of laser in the 1960'ies. Immediately after the first lasers became available, there was a flood of theoretical and experimental studies on the ablation process, and a few years later it was demonstrated that intense laser radiation could be utilized in thin-film deposition. This application of laser ablation is called pulsed laser deposition (PLD).

Among the large number of processes to fabricate thin films of materials, PLD has emerged as a unique method to obtain epitaxial superconductor thin films of multi-component oxides. The first successful deposition of a YBCO film was made in 1987, soon after the superconductivity of the material was reported. A laser beam enters a vacuum chamber through a window and impinges on the target material to

be deposited. The 20 to 30 nanosecond wide laser pulse is focused to an energy density of 1 to 5 J/cm^2 to vaporize a few hundred angstroms of surface material. The vapour contains neutral atoms, positive and negative ions, electrons, molecules and molecular ions, free radicals of the target material in their ground and excited states. These particles acquire kinetic energy of 1 to 5 eV and move in the direction perpendicular to the target [15]. They deposit on a substrate generally heated to a temperature to grow crystalline film of exactly the same composition as the target.

2.2.1 Laser -Target Interaction

The interaction between laser pulses and the target depends strongly on the intensity of the incoming laser beam. In PLD, the intensity is on the order of 10^8-10^9 W/cm^2 corresponding to a pulse duration of a few nanoseconds. Therefore, there is enough time for the pulses to absorb, heat the target surface, and, finally, lead to the removal of matter. There are many different mechanisms through which energy can be transferred to the target and the most important ones are briefly discussed below the term sputtering is used to describe the different phenomena.

2.2.1.1 Collisional Sputtering

The momentum of the incident beam is transferred to the target, which results in an ejection of particles from the surface. The mechanism is of great importance if the incoming beam consists of massive particles, such as ions. In the case of photons, the maximum transfer of energy (E_2) is negligible as shown in the following equation [3].

$$E_2 = \frac{E_1^2}{M_2} \times 2.147 \times 10^{-9} + \frac{4M_1M_2E_1}{(M_1 + M_2)^2} \quad \text{.....(1)}$$

where E_1 is the energy of the incoming particles, and $M_1$and M_2 are the masses of the incoming and the target particles, respectively.

2.2.1.2 Thermal Sputtering

The absorbed laser beam melts and finally vaporizes a small area of the target material. The surface temperature of the target is typically above the boiling point of the ablated material but the observed material removal rates typically require even higher temperatures [3].Therefore, the mechanism can only partly explain the formation of the ablation cloud.

2.2.1.3 Electronic Sputtering

The principal interaction mechanism of a laser pulse with the target. The mechanism is not a single process but rather a group of processes, all of which have the common feature of involving some form of excitations and ionizations. The incident photons strike the target, producing electron-hole pairs and electronic excitations in a femtosecond timescale. After a few picoseconds, the energy is transferred to the crystal lattice, and during the laser pulse, within a few ns, a thermal equilibrium between the electrons and the lattice is reached. This leads to a strong heating of the lattice and, with continued irradiation, to a massive particle emission from the surface [3].

2.2.1.4 Hydrodynamic Sputtering

The process in which the target surface melts forming small droplets of material which are finally expelled from the surface [3].

2.2.1.5 Exfoliational Sputtering

This takes place when the fluence on the target is sufficiently high. Owing to repeatedly occurring thermal shocks and intense laser irradiation, the surface begins to crack since thermal stresses do not have time to relieve by melting. As a consequence of this kind of behaviour, an uneven surface with cone-shaped features is formed [3]. These cones are considered to be partly responsible for the particulates frequently observed on the film surface [16]. In addition to particulates, cone formation can also change the direction of the plume towards the incoming beam and decrease the deposition rate from 1 Å/pulse to approximately 0.2 Å/pulse after a few hundred pulses [17].

2.2.2 Effects of Process Parameters

2.2.2.1 Laser Fluence

For a chosen material and a fixed laser wavelength, the laser fluence on the target has the most significant effect on the particular size and density. The laser fluence can be varied by varying the laser power or the laser spot size. At constant laser power, the particulate number density is usually higher with tighter focus. In general, there exists a threshold laser fluence, below which the particulates are barely observable. For example, in the case of high Tc YBCO material, the threshold laser fluence for the occurrence of particulates is about 0.9 J/cm2 when a XeCl (308 nm) excimer laser with 20 ns pulse duration is used [18]. Above the threshold laser fluence, the particulate number density increases rapidly with increasing fluence.

2.2.2.2 Laser Wavelength

The wavelength of the laser has a significant effect on the yield of the ablated particles. Usually, at shorter wavelengths (UV region) the reflectivity of most materials is much lower than at long infrared wavelengths. When the reflectivity

decreases, a larger part of a laser pulse is absorbed, which increases the number of sputtered particles. Another advantage is that also the absorption coefficient is larger in the UV region such that the beam energy is absorbed in a thin surface layer and the ablation occurs more efficiently [3].

2.2.2.3 Ambient Oxygen Pressure

Ambient oxygen scatters and attenuates the plume, changing its spatial distribution, the deposition rate, and the kinetic energy distribution of the different species. In addition, reactive scattering results in the formation of molecules or clusters which are essential for the proper stoichiometry and oxygen content of the film. At a typical YBCO deposition pressure (0.2-0.3 mbar oxygen), only 20 % of the initially ablated material condenses on the substrate [19]. Raising of the oxygen pressure results in an increase in the fluorescence, sharpening of the plume boundary and the shock front, slowing of the plume relative to the propagation in vacuum, and a higher spatial confinement of the plume [3]. Oxygen pressure has also an influence on the length of the plume and it is often the easiest parameter that can be slightly modified during the deposition. Process parameters have to be adjusted in such a way that the plume tip touches the substrate.

2.2.2.4 Target to Substrate Distance (T-S distance; d_{TS})

The specific effects of d_{TS} and ambient pressure are interrelated. Due to the increased collisions between the laser-produced plume and the background gas, the plume dimension decreases as the background gas pressure increases.

$$L\alpha\left(\frac{E}{P_O}\right)^{\frac{1}{3\gamma}} \quad \text{.....(2) [20]}$$

L Length of the plume

E Laser pulse energy

P_O Background gas pressure

γ Ratio of specific heats of the elements in the plume

When the T-S distance is much smaller than L, there is no marked difference in particular size and the density. Once the substrate is located far beyond the L, the adhesion to film material to the substrate is poor. [20].

2.2.2.5 Substrate Temperature (T_{sub})

In the case of PLD-Y123 films, the *a*-axis oriented growth becomes dominant with decreased T_{sub} [21]. Izumi *et al* [22] explained the mechanism from *c*- to *a*-axis orientation change based on the adatom kinetics, namely, high surface mobility of adatoms leads to the *c*-axis orientation of Y123 films and the low surface mobility causes the *a*-axis orientation. A schematic view of adatom migration on RE123 (RE = Y, Nd, Sm etc) film is illustrated in Figure 2.4. For the *c*-axis oriented growth, the adatoms of each element should climb the steps and migrate a long distance before finding their stable sites, while a short distance migration of adatoms is enough for *a*-axis oriented growth. This mechanism of orientation is consistent with the results of the conventionally produced PLD-Y123 films [23].

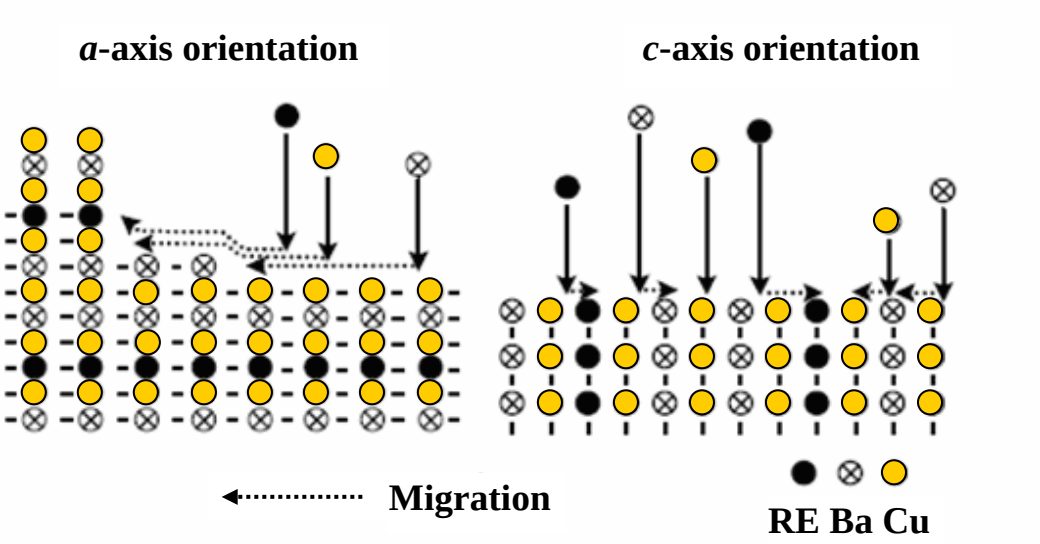

Figure 2.4: A schematic drawing of the orientational behaviour depending on the surface mobility of adatoms.

2.2.3 Comparison of PLD Method with Other Methods

Advantages

- The film is deposited with the same composition as the target. Therefore it is easy to control the stoichiometry of the film by changing the atomic constituents of the target.
- The energy at the target can be controlled independently of the process pressure and gas mixture.
- The apparatus is simple and provides high deposition rates.

Disadvantages

- The pulsed deposition has large impact on the morphology of the sample and usually micrometre sized droplets are formed on the surface of the deposited film. [24]
- PLD is limited to small area depositions due to sharply pointed geometry of the plume.

2.3 References

(1) T. Davis, C. Christopher, Lasers and Electro-Optics, Cambridge University Press, New York, 133-136 (1996).

(2) D.Y. She, J.K. Sahu, W.A. Clarkson, Opt.Lett. 31, 754 (2006).

(3) D.B. Chrisey, G.K. Hubler, Pulsed Laser Deposition of Thin Films, John Wiley and Sons, Inc., New York, 24-30 (1994).

(4) X.C. Wen, W.Z.Yi, H.K. Na, L.D. Hua, Z.Y. Dong, Chinese Phys. Lett. **26,** 014213 (2009).

(5) A.B. Borisov, X. Song, F. Frigeni, Y. Dai, Y. Koshman, W.A. Schroeder, J. Davis, K. Boyer, C.K. Rhodes, J. Phys. B: At. Mol. Opt. Phys. 35 (2002).

(6) I. diaz, M. santos, J.A.Torresano, M.Castillejo, M. jadraque, M. martin, M. oujja, E. rebollar, Appl. Phys. A 85, 33–37 (2006)

(7) N. Michael, R. Ashfold, F. Claeyssens, M. Gareth, J. Simon, Chem. Soc. Rev.**,** 33**,** 23 – 31(2004).

(8) D. Dijkkamp, T. Venkatesan, X. D. Wu, S. A. Shaheen, N. Jisrawi, Y.H.Min-Lee, W. L. McLean, M. Croft, Appl. Phys. Lett. 51, 619 (1987).

(9) D. Basting, G. Marowsky, Excimer Laser Technology, Springer Berlin Heidelberg, Germany, 385-397 (2005).

(10) M. Allmen, A. Blatter, Laser-Beam Interactions with Materials, Springer-Verlag, Berlin (1997).

(11) H.C. Lee, Y.P. Kim, Optics & Laser Technology, 40, 901-905 (2008).

(12) W. Zendzian, J.K. Jabczynski, J. Kwiatkowski, Optics & Laser Technology, 40, 441-444, (2008).

(13) Y.F. Chen, Y.P. Lan, Appl. Phys. B, 79, 29–31 (2004).

(14) Nd:YAG Laser System LS-2147 User's Manual, Minsk 220012, Republic of Belarus (2007).

(15) M.S. Hegde, Proc. Indian Acad. Sci. (Chem. Sci.), 113, 445–458 (2001).

(16) S. Proyer, E. Stangl, M. Borz, B. Hellebrand, D. Bäuerle, Physica C 257, 1 (1996).

(17) S.R. Foltyn, R.C. Dye, K.C. Ott, E. Peterson, K.M. Hubbard, W. Hutchinson, R.E. Muenchausen, R.C. Estler, X.D. Wu, Appl. Phys. Lett. 59, 594 (1991).

(18) G.A Farnan, M.P. McCurry, C.C. Smith, R.J. Turner, D.G. Walmsley, Supercond. Sci. Technol. 13, 262-272 (2000).

(19) D.Q. Shi, R.K. Ko, K.J. Song, J.K. Chung, S.J. Choi, Y.M. Park, K.C. Shin, S.I. Yoo , C. Park, Supercond. Sci. Technol. 17**,** S42-S45 (2004).

(20) R.F. Wood, J.N. Leboeuf, K.R. Chen, D.B. Geohegan, A.A. Puretzky, Appl. Surf. Sci. 127-129, 151 (1998).

(21) M. Mukaida, S. Miyazawa, Japan. J. Appl. Phys. 32 4521(1993).

(22) H. Izumi ,PhD Thesis Tokyo Institute of Technology, Tokyo (1992).

(23) Y. Ichino, Y. Yoshida, Y. Takai, K. Matsumoto, H. Ikuta, U. Mizutani, Supercond. Sci. Technol. 17, 775–780 (2004).

(24) T. Kusumori, H. Muto, Physica C 227-244, 351 (2001).

CHAPTER 3

Texture and Surface Morphology of (Y,Ho)BCO Films on MgO Substrates

3 Texture and Surface Morphology of (Y,Ho)BCO Films on MgO Substrates

3.1 Experimental Procedures

3.1.1 Preparation of ($Y_{1-x}Ho_x$)BCO Targets

- Commercially available powders of Y_2O_3, Ho_2O_3, $BaCO_3$ and CuO were thoroughly mixed in the desired proportions: x=0, 0.3, 0.5, 0.7 and 1, using a standard ball mixer. (hand mixing using a mortar and pestle is believed to have resulted in poor target quality.)
- Powder mixtures were calcined at 850°C for 10 hr and small content was separated from each calcined sample.
- The calcined powder mixtures were pressed into pellets with the dimensions of 30 mm diameter and 5mm thickness, applying a pressure of 4.5 kgf/cm^2 using hydraulic oil press.
- The pellets and separated calcined powder samples were sintered at 950°C for 10 hr.

3.1.2 Examination of Y:Ho Ratio Dependence of Lattice Constants

- X-ray powder diffraction (XRD: θ-2θ scan) was carried out for small fragment of each sintered powder sample.

3.1.2.1 X-ray Powder Diffraction (XRD: θ-2θ Scan)

X-Ray powder Diffraction analysis is a powerful method by which X-Rays of a known wavelength are passed through a sample to be identified in order to identify the crystal structure. The wave nature of the X-Rays means that they are diffracted by the lattice of the crystal to give a unique pattern of peaks of 'reflections' at

differing angles and of different intensity, just as light can be diffracted by a grating of suitably spaced lines. The diffracted beams from atoms in successive planes cancel unless they are in phase, and the condition for this is given by the BRAGG relationship.

$$n\lambda = 2dSin\theta \quad \text{.....(4)}$$

λ, wavelength of the X-Rays

d, distance between different planes of atoms in the crystal lattice.

θ, angle of diffraction.

Figure 3.1: Model JEOL JDX-3500 X-ray diffractometer.

The X-Ray detector moves around the sample and measures the intensity of these peaks and the position of these peaks [diffraction angle 2θ].

Electrons of typically 35-40 KeV are directed at a copper target and radiations with following wavelengths are emitted [1].

$CuK_{\alpha 1}$ - 1.540 Å

$CuK_{\alpha 2}$ - 1.544 Å

CuK_{β} – 1.392 Å

A Ni foil filter is often used to attenuate CuK_{β} radiation [1].

Sample Preparation

Material was ground by hand in a pestle & mortar sufficiently fine. Then small quantity of powder was put on the sample holder (cleaned glass plate) and made it as a layer adding few drops of ethanol. Proper sample preparation causes correctly orientated crystallites which are fulfilled the Bragg equation for each value of *d*.

Operation Method of the X-Ray Diffractometer

The scan was carried out by CuK_{α} radiation and X-Ray detector was set to move in the range of 2θ = 5-60° at increments of 0.04° with a count time of 1 second. The data were shown in the computer screen; the intensity of the X-rays is measured on the Y axis, and increasing values of 2θ are shown on the X axis.

- Valves of d_{200} and d_{600} were calculated by considering the 2θ valve of (200) and (006) peaks appeared in XRD: θ-2 θ profile.

3.1.3 Measuring the Laser (FH) Energy Density (E_d)

- Required pump energy (≤ 65J) was set in the remote control and turned on the laser [2].
- Thick white paper screen was put in front of the output laser beam and burned spot was taken on it.
- The area of the spot was calculated (A)
- The head of Model H410D energy meter [3] was set up in front of the output laser beam (the distance between laser emitter and head of energy meter should be less than 50 cm)
- The position of the energy meter head was aligned in the way that radiation falls onto the centre of the head and energy valve (E) was recorded.
- Laser energy density was calculated as, $E_d = (E / A)$

3.1.4 Preparation of Substrates for Deposition.

- 0.5 mm thick mirror polished (100) MgO and STO single crystals (10 mm x 5 mm) were used as substrates.
- Substrates were immersed in 1M HNO_3 for 10 min. and washed by water and Acetone.
- Pre-annealing treatment was conducted at 850 °C for 6 hours in air.

3.1.5 Film Deposition by PLD

In all experiments, FH laser (wave length: 266 nm) was used with pulse repetition rate (f) of 10Hz and pulse duration (FWHM) of 18 ns. Target rotation speed of 20 rpm and target-to-lens distance of 50 cm were kept constant. Prior to deposition, the deposition chamber was evacuated to 1x 10^{-2} Pa with a turbo pump.

3.1.6 Studying the Effect of Substrate Temperature on the Texture Quality

In this case, YBCO ($x = 0$) target was selected. Set of experiments were conducted by setting the T_{sub} in the range of 670-790 °C and it was increased by 10°C. Other PLD parameters were kept constant as follows;

O_2 pressure, P: 20 Pa

T-S distance, d_{TS}: 5 cm

Energy density, E_d: 2 Jcm^{-2}

Deposition time, t : 30 min

3.1.6.1 Analysis of c-axis Orientation

c-axis orientation of prepared films was assessed by means of XRD: θ-2θ scan. (The procedure mentioned in section 3.1.2.1 was followed).

3.1.6.2 Analysis of In-Plane Texture

The texture possesses high in-plane texturing, when mis-orientation angle, θ is very small.

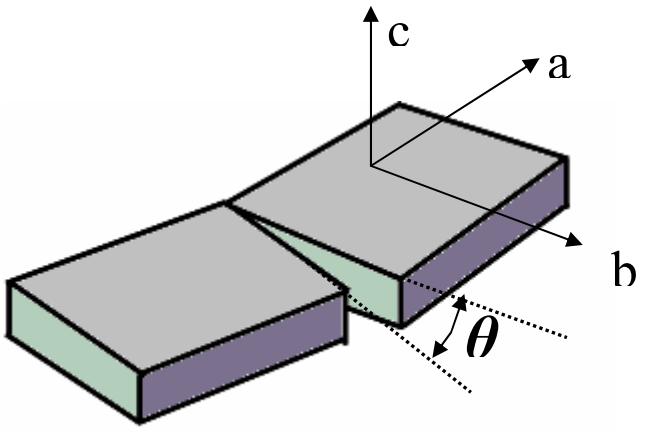

Figure 3.2: In-plane mis-oriented grains.

- In-plane texturing was assessed on prepared YBCO samples by conducting XRD ϕ-scan around YBCO (103) plane.
- The parameters were set as 2θ=32.5° (2θ, corresponds to (103) plane of YBCO) and α=45 (Figure 2.5) Rotating speed of the sample holder was adjusted as 0.5°/sec.

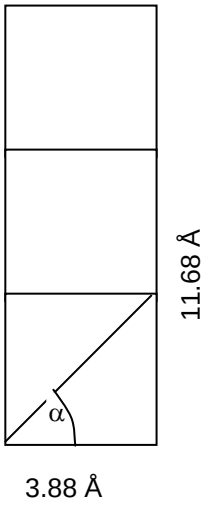

Figure 3.3: Simple side view of YBCO crystal structure

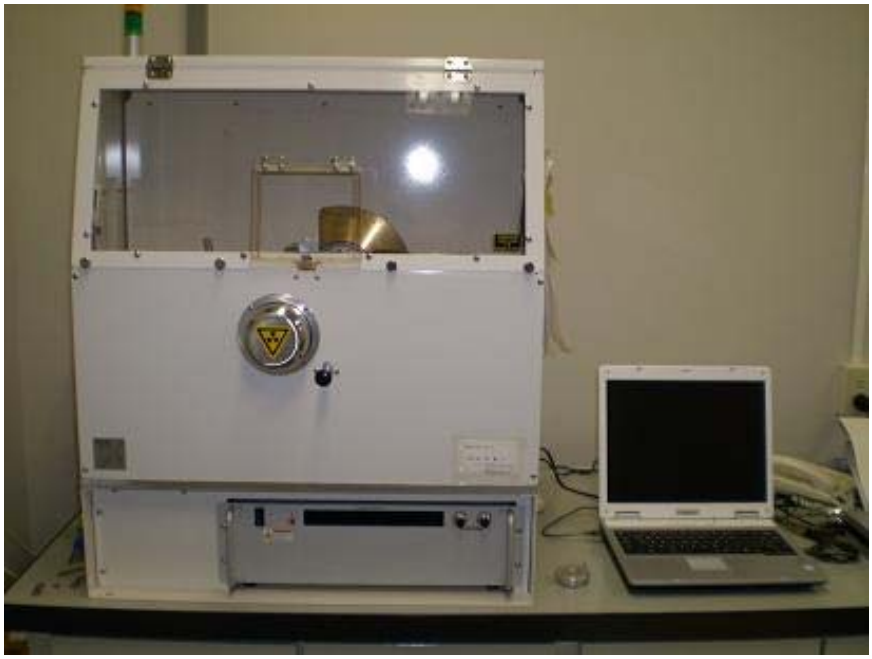

Figure 3.4: X-Ray Diffractometer used for in-plane texture assessment.

3.1.7 Studying the Influence of T-S Distance and O_2 Pressure on the Texture Quality

YBCO (x=0) thin films were deposited on MgO substrates, setting T-S distance, d_{TS} at 40 to 50 mm and changing oxygen gas pressure, P in the range of 16-26 Pa. Other PLD parameters were kept constant as follows;

Energy density, E_d : 2 Jcm^{-2}

Deposition time, t : 30 min

Substrate temperature, T_{sub} : 757 °C

Texture quality of prepared films was assessed by means of XRD: θ-2θ scan. (The procedure mentioned in section 3.1.2.1 was followed).

3.1.8 Studying the Influence of T-S Distance and Energy Density on the Texture Quality

Set of experiments were carried out to prepareYBCO (x=0) films on MgO substrates, setting d_{TS} at 40 to 50 mm and changing E_d in the range of 1.7-2.3 Jcm^{-2}.

Other PLD parameters were kept constant as follows;

Deposition time, t : 30 min

Substrate temperature, T_{sub}: 757 °C

O_2 Pressure, P : 20 Pa

Texture quality of prepared films was assessed by means of XRD: θ-2θ scan. (The procedure mentioned in section 3.1.2.1 was followed).

3.1.9 Observing the Surface Morphology

The scanning electron microscope (SEM) is a type of electron microscope that images the sample surface by scanning it with a high-energy beam of electrons in a raster scan pattern. The electrons interact with the atoms that make up the sample producing signals that contain information about the sample's surface morphology and composition. The types of signals produced by an SEM include secondary electrons, back scattered electrons (BSE), characteristic x-rays, light (cathod-luminescence), specimen current and transmitted electrons.

Sample Preparation

Nonconductive specimens tend to charge when scanned by the electron beam, and this causes scanning faults. Therefore non –conductive thin film samples were coated with an ultrathin gold coating using Model JFC-1200 fine coater. (Coating is deposited on the sample by low vacuum sputtering method)

- The film surface with scattered particles was observed by means of Model JEOL JSM-5310 SEM machine (Figure 3.5).
- The particle density of each film was calculated by counting the number of particles, using computer software.

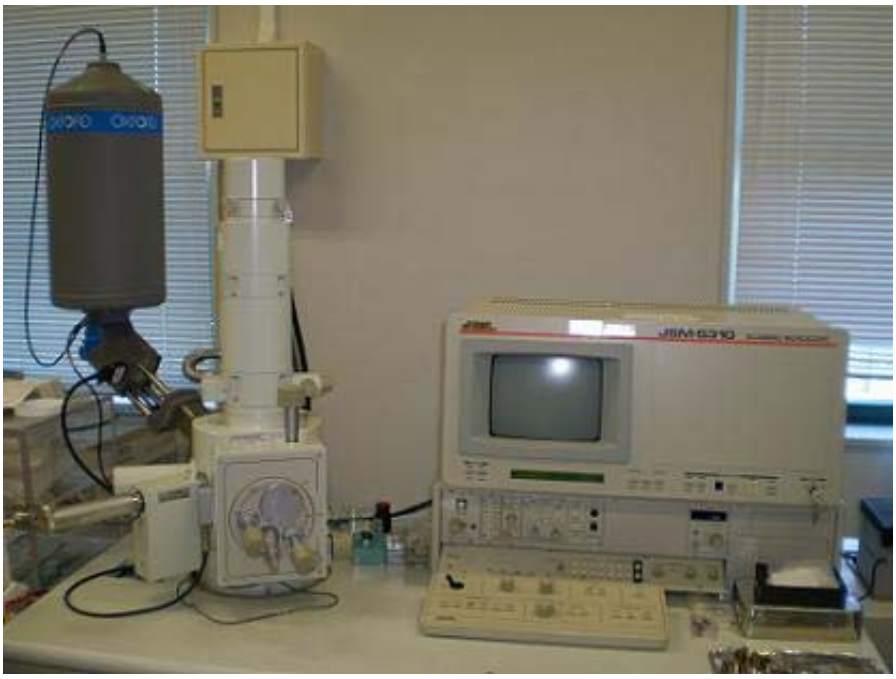

Figure 3.5: Model JEOL JSM-5310 Scanning Electron Microscope (SEM)

3.2 Results and Discussion

3.2.1 Y/HO Ratio Dependence of Lattice Constants

Samples of x=0 (YBCO) can be synthesized with varying crystal structure depending on the oxygen content. This is denoted by the (z) in the chemical formula, $YBa_2Cu_3O_z$. For $z > 6.6$, Cu-O chains along the b-axis of the crystal are formed and elongation of the b-axis changes the structure to orthorhombic [4]. When $z \sim 7$, optimum superconducting properties occur with lattice parameters of a=3.8227 Å, b = 3.8872 Å and c = 11.6800 Å [5].

This study examined the Y:Ho ratio dependence of lattice constants. A small fragment of each target (x=0, 0.3, 0.5, 0.7 and 1) was pulverized and subjected to powder XRD measurement. Parameters a and c/3 (b is almost equal to c/3) of powder samples with different x values were calculated by means of XRD: θ-2 θ profile considering 200 and 006 peaks (Figure 3.6). The results showed that all samples were not fully oxidized and their crystallographic structure was tetragonal. According to figure 3.6, the Y:Ho ratio does not affect to the lattice constants. This is because the Y^{3+} and Ho^{3+} have almost the same value of ionic radius at 8-fold coordination (Y^{3+}: 0.1019 nm, Ho^{3+}: 0.1015 nm [6]).

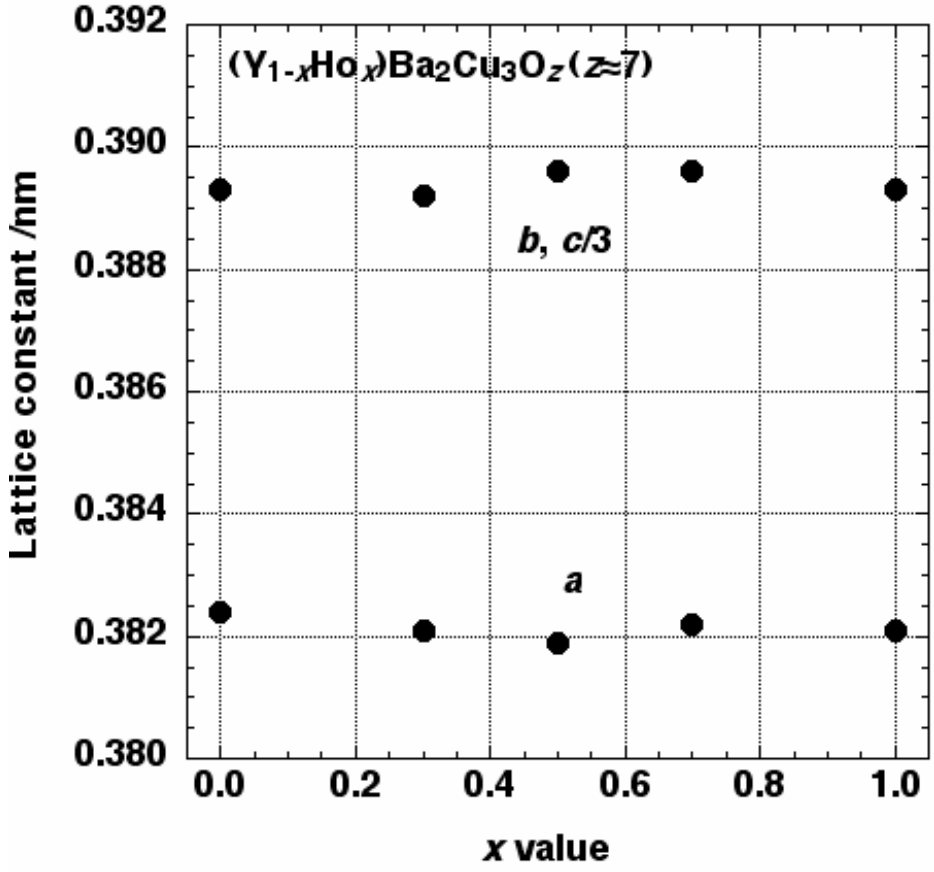

Figure 3.6: Y/Ho ratio dependence of lattice constants

3.2.2 Texture Quality of (Y,Ho)$Ba_2Cu_3O_z$ Films

REBCO coated conductors, the so-called second generation superconducting tapes, which are based on REBCO thin film technology also have great applications [7] in carrying large superconducting currents. According to this viewpoint, critical current density (J_c) is the most crucial characteristic in superconductor thin films. In-plane texture plays a significant role in enhancing J_c. For YBCO thin films, to achieve high J_c, in-plane mis-orientation angle, θ <10º [8].

Two types of c-axis oriented REBCO films are deposited on (100) MgO single-crystal substrates; {001}<100> texture in which {001} planes of both REBCO and MgO are aligned in the same direction of <100> ("cube-on-cube" configuration) and

{001}<110> texture which contains {001} REBCO planes rotated by 45° from the direction of <100> ("45° rotated" configuration). All films with different x values are highly c-axis oriented (Figure 3.7). Figure 3.8 gives XRD ϕ-scan profiles for the films deposited using the "optimized" parameters (Table 3.1) , which clearly show that all of the "optimized" films have sufficient in-plane texture except for x=0.7. In this film, "cube-on-cube" grains were dominant but a few amounts of "45° rotated" grains were also contained.

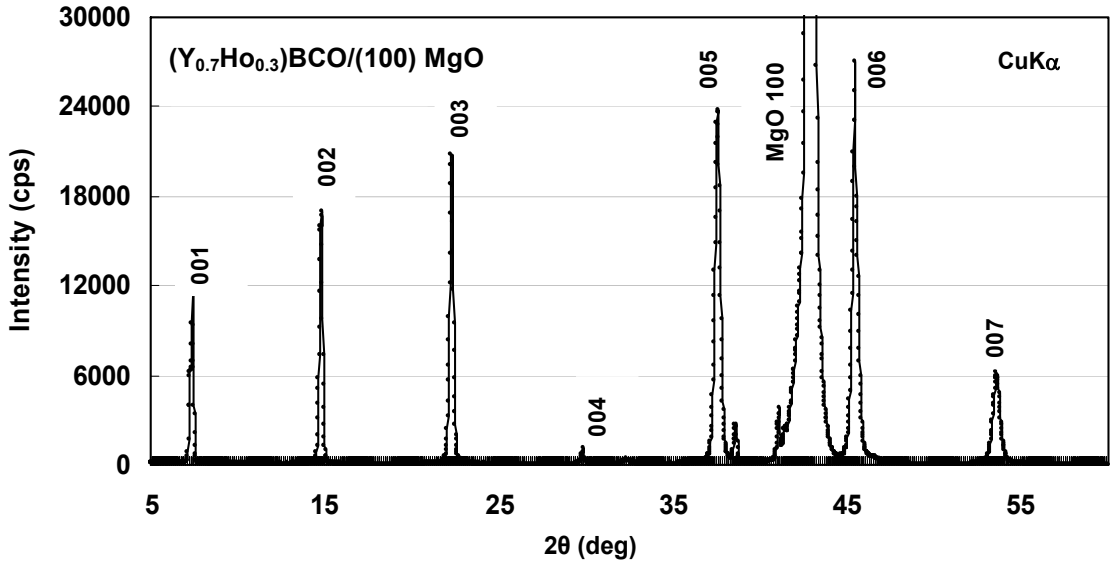

Figure 3.7: XRD: θ-2θ scan for sample x= 0.3

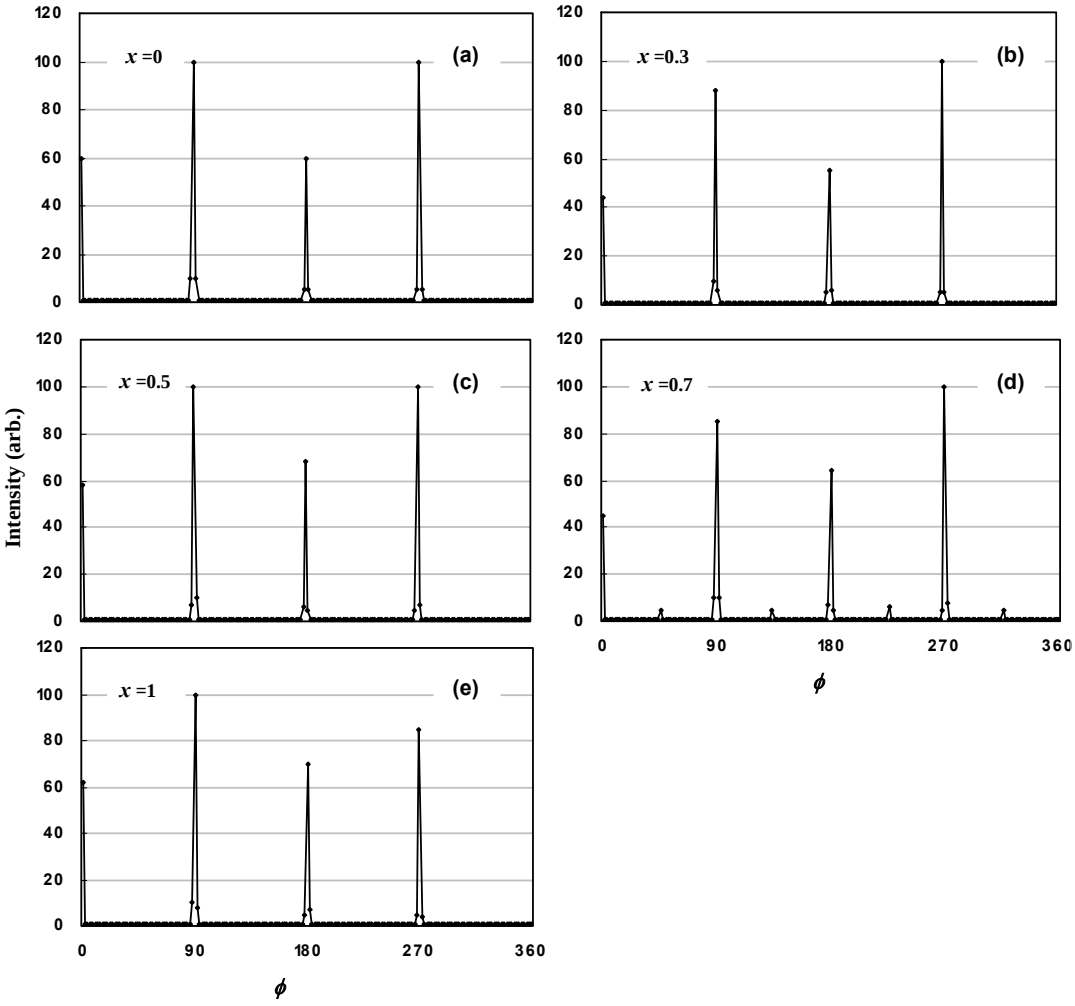

Figure 3.8: XRD ϕ-scan profiles for samples of x=(a) 0, (b) 0.3, (c) 0.5, (d) 0.7 and(e) 1. prepared on MgO single crystal substrates.

Table 3.1: Optimized PLD parameters for $(Y_{1-x}Ho_x)Ba_2Cu_3O_z$ films on 100 MgO substrates

Composition	$x = 0$	$x = 0.3$	$x = 0.5$	$x = 0.7$	$x = 1$
Substrate temp. T_{sub} (˚C)	757	762	770	776	783
O_2 pressure, P (Pa)	20	20	22	22	20
T-S distance, d_{TS} (mm)	45	45	45	50	50
Energy density, E (Jcm^{-2})	2.0	2.0	2.0	1.9	1.9
Deposition time, t (min)	30	30	30	30	30

As can be seen in Table 3.1, T_{sub} is the most crucial parameter in preparing c-axis oriented films with cube-on-cube configuration and it must be increased with Ho content. One obvious reason for this change in T_{sub} is the high atomic weight of Ho (164.93) relative to Y (88.91). More kinetic energy is required for Ho atoms to move towards the cluster [9,10] on the substrate surface.

3.2.3 Influence of Interrelation of T-S Distance and Oxygen Pressure on Texture Quality

Since it is empirically well known that the texture quality is strongly dependent on distance between plume top and substrate, d_{TS} is significantly important parameter and should be optimized according to plume dimension which is, however, directly affected by p and E. Due to the increased number of collisions between laser pulse and the background gas, the plume dimension decreases as p increased [11]. Increased E produces longer plume because the initial velocity of the particles is

higher [12,13]. Therefore, among various PLD parameters, Fig. 3.9(a) especially summarizes the influence of d_{TS} and p on the texture quality for the films of x=0 (YBCO). Other parameters than d_{TS} and p were kept constant at the optimal values shown in Table 3.1. YBCO film (x=0) was selected because present experimental results showed that Y:Ho ratio does not affect the texture quality. It is shown that relatively low p tends to result in a-axis oriented films in which <001> of YBCO is parallel to substrate surface while amount of c-axis oriented grain increases as p increases. Within our experimental setup, p values of 20 and 22 Pa with d_{TS} values of 45 mm were selected as the most effective combinations for the preparation of c-axis oriented YBCO films.

3.2.4 Influence of Interrelation of T-S Distance and Energy Density on Texture Quality

The interrelation of T-S distance and laser energy density dependence of the texture quality of the YBCO films (x=0) was studied. Fig. 3.9(b) especially summarizes the influence of d_{TS} and E for the films of x=0. It is shown that high E tends to produce a-axis oriented films while amount of c-axis oriented grain increases as E decreased. E of 2 Jcm^{-2} with d_{TS} of 45 mm was selected as the best combination to prepare c-axis oriented YBCO films. Plume length corresponding to these combinations was roughly estimated as 35 mm.

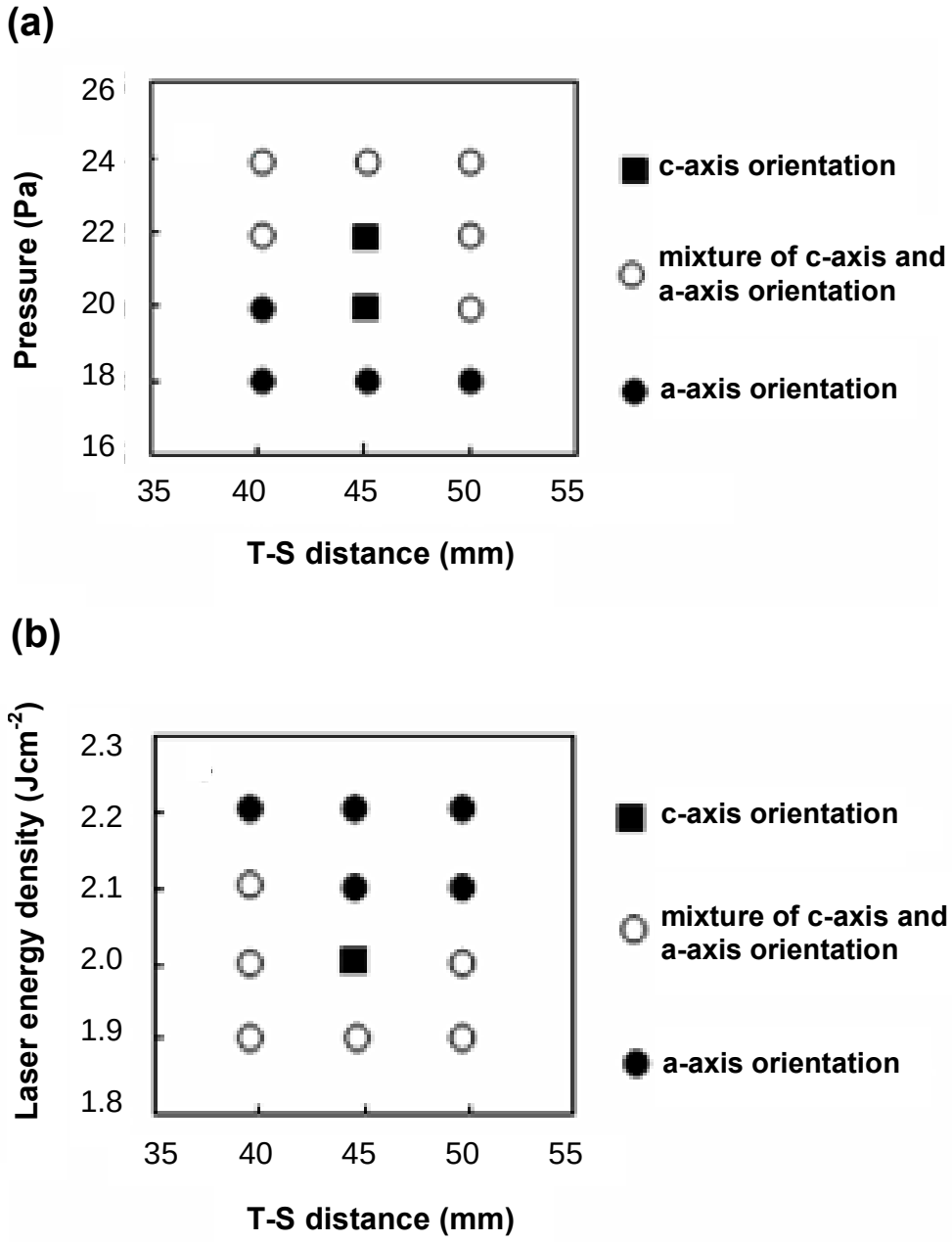

Figure 3.9: Influence of (a) d_{TS} and p and (b) d_{TS} and E on the texture quality.

3.2.5 Examination of Surface Morphology

Previous studies have shown that precipitate formation is very sensitive to the PLD conditions [14]. A homogeneous uniform laser output is required for good quality deposition work. Hot spots and deviations from uniformity can result in non-stoichiometric films as well as undesirable particulate formation. From the viewpoint of electronic device application, the presence of precipitates is one of the main obstacles to the fabrication of Josephson tunnel junctions. But our intention is to extend this work towards the coated conductor fabrication. Therefore controlling the precipitate formation sufficiently is adequate for coated conductors. These particulates can be classified into two major types: small droplets (typical size 0.2-3 μm) and large irregularly-shaped outgrowths (diameters up to more than 10 μm) [15].

In this study, surface morphology of prepared films was analyzed using a scanning electron microscope (SEM). It was clearly observed that small droplets of 0.2- 0.8 μm were deposited on the film surface of all samples: x=0, 0.3, 0.5, 0.7 and 1 (Figure 3.10-3.14). The particle density was calculated by counting the number of particles, using computer software. Five SEM photographs with the same magnification were used for each sample and particle densities of samples were calculated as shown in table 3.2.

Table 3.2: Particle density of $(Y_{1-x}Ho_x)Ba_2Cu_3O_z$ films

Composition	$x = 0$	$x = 0.3$	$x = 0.5$	$x = 0.7$	$x = 1$
Particle density Dx10^5 cm^{-2}	84	126	133	139	95

Those results revealed that particle densities of all samples were nearly the same as the PLD-YBCO films fabricated using ArF excimer laser (refer Fig.1 in Ref.[10]). Among these samples, x=0 (YBCO) and x=1 (HoBCO) showed lower particle densities relative to other samples, but exact reason for this difference has not been revealed yet.

However these particles are believed to have originated from two sources. One is the droplets which come directly from the target because of the explosive laser-ablation process [16, 17]. The other is the precipitates segregated from the YBCO matrix due to off stoichiometry [18]. Therefore precipitates such as CuO and $BaCuO_2$ [19] could have been deposited on the film.

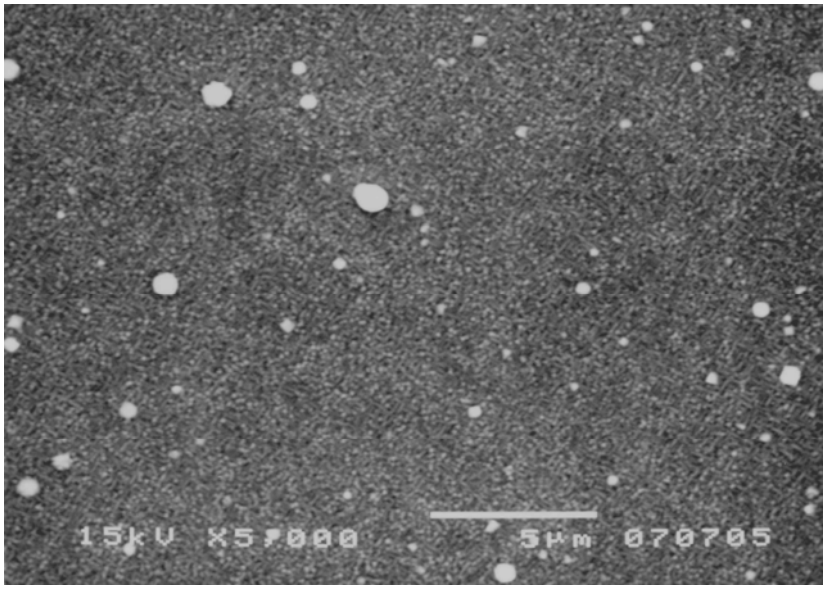

Figure 3.10: SEM image of surface morphology for sample x= 0.

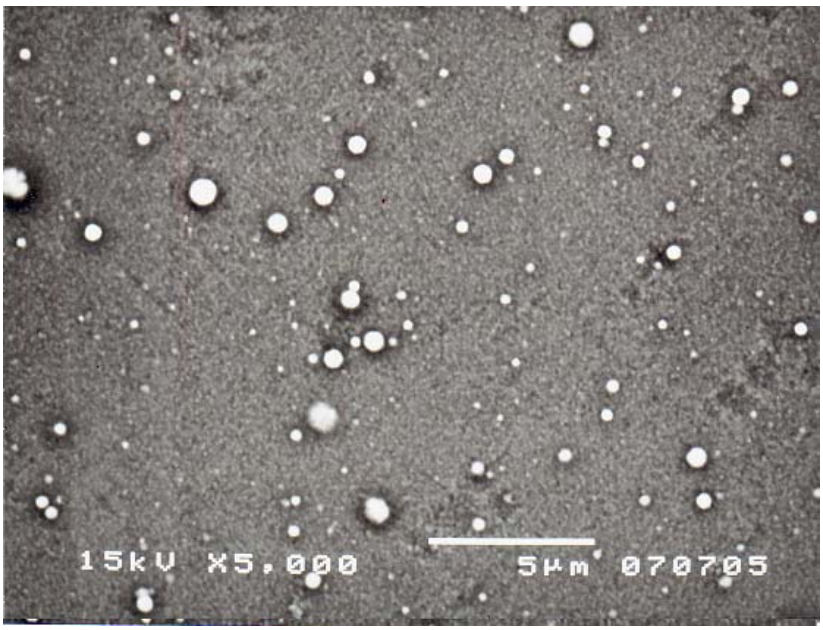

Figure 3.11: SEM image of surface morphology for sample x= 0.3.

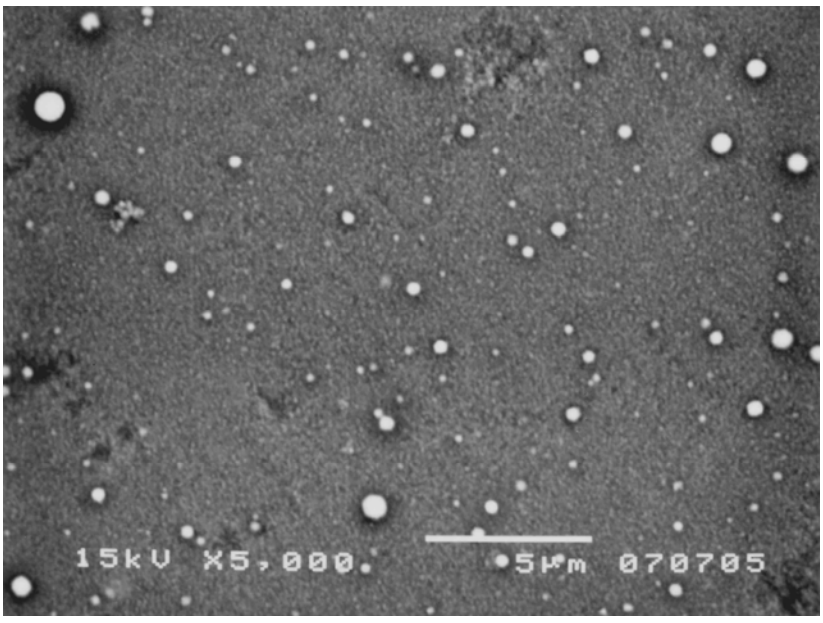

Figure 3.12: SEM image of surface morphology for sample x= 0.5

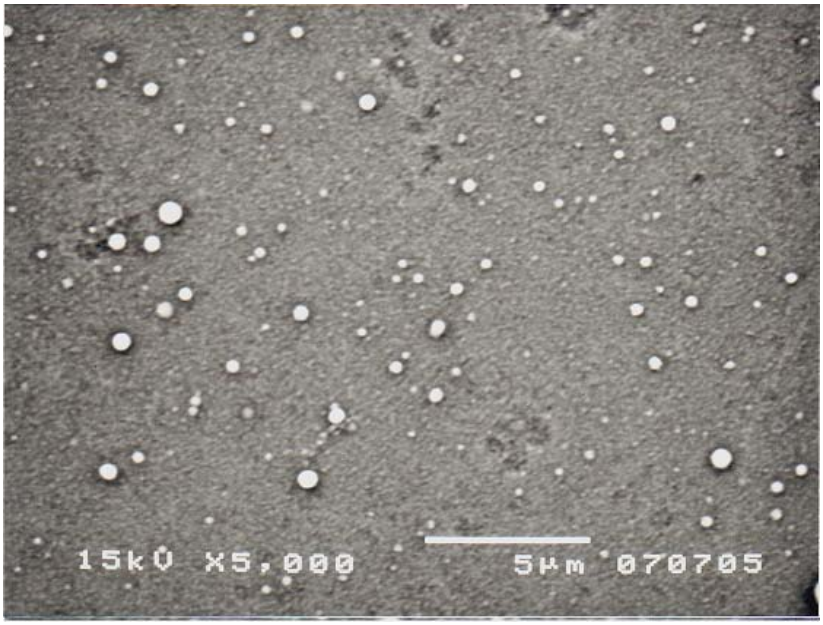

Figure 3.13: SEM image of surface morphology for sample x= 0.7

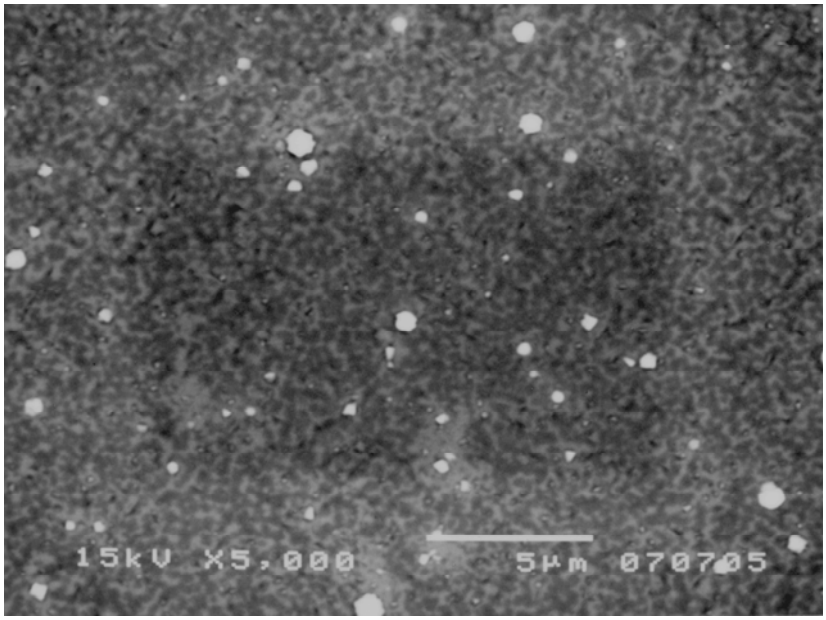

Figure 3.14: SEM image of surface morphology for sample x= 1

3.3 References

(1) D.L Bish, J.E Post, Modern Powder Diffraction, Min. Soc. America Reviews in Mineralogy, U.S.A, 20, 369 (1992).

(2) Nd:YAG Laser System LS-2147 User's Manual, Minsk 220012, Republic of Belarus 2007

(3) Models H410 and H410D Laser Power and Energy Meters Setup and Operating Procedures

(4) F.J. Owens, C.P. Poole, The New Superconductors, Plenum Press., New York, 143 (1996).

(5) K. Fossheim, A. Sudb, Superconductivity Physics and Applications, John Wiley and Sons, Inc., New York, 44 (2004).

(6) R. D. Shannon, Acta Cryst. **A32**, 751 (1976).

(7) Y. Shiohara, M. Yoshizumi1, T. Izumi, Y. Yamada, Supercond. Sci. Technol.21 034002 (2008).

(8) D.Dimos, P. Chaudhari, J. Mannhart, Physical Review B. 41, 7 (1990).

(9) Huhtinen, P. Paturi, E. Lahderanta, R. Laiho, Supercond. Sci. Technol.12, 81 (1999).

(10) S. Amoruso, M. Angeloni, G. Balestrino, N. Boggio, R. Bruzzese, P.G. Medaglia, A. Tebano, M. Vitiello, X. Wang, Applied Surface Science, 247, 64-70 (2005)

(11) J.P. Gong, M. Kawasaki, K. Fujito, R. Tsuchiya, M. Yoshimoto, H. Koinuma, , Phys. Rev. B 50, 3280 (1994).

(12) T.Haugen, P.N. Barnes, R. Wheeler, F. Meisenkothen, M. Sumption, Nature 430, 867, (2004). .

(13) A.P. Malozemoff, J. Mannhart, D. Scalapino, Phys. Today, 58, 41 (2005).

(14) M.S. Hegde, Proc. Indian Acad. Sci. (Chem. Sci.), 113, 445–458 (2001).

(15) S. Proyer, E. Stangl, M. Borz, B. Hellebrand, D. Bauerle, Physica C 257, 1 (1996).

(16) F. Zupanic, T. Boncina, D. Pipic, V.H. Bartolic, Journal of Alloys and Compounds, 465, 197-204 (2008).

(17) X.Z. Liu, S.M. He, D.J. Wu, K.Y. Duan, Y.R. Li, Physica C 147-153, 433 (2006).

(18) T. Kusumori, H. Muto, Physica C, 227-244, 351 (2001).

(19) X.F. Zhang, H.H. Kung, S.R. Foltyn, Q.X. Jian, E.J. Peterson, D.E. Perterson, J. Mater. Res. 14, 1204 (1999).

CHAPTER 4

Current Characteristics of (Y,Ho)BCO Films on STO Substrates

4 Current Characteristics of (Y,Ho)BCO Films on STO Substrates

4.1 Experimental Procedures

4.1.1 Analyzing the Texture quality

PLD condition was optimized in order to fabricate highly c-axis oriented films with improved in-plane texture. c-axis orientation and in-plane texture were assessed by conducting XRD: θ-2θ scan and ϕ-scan (around (Y,Ho)BCO (102) plane) respectively, following the procedures explained in sections 3.1.2.1 and 3.1.6.2.

4.1.2 Conducting the Oxygen Annealing Treatment

After complete the deposition process, O_2 annealing was conducted inside the deposition chamber following the profile shown in Figure 4.1. Annealing temperature and soaking time at that temperature were adjusted until optimum annealing profile which gives the higher T_c is achieved. During the annealing process, O_2 pressure was kept at 10^5 Pa.

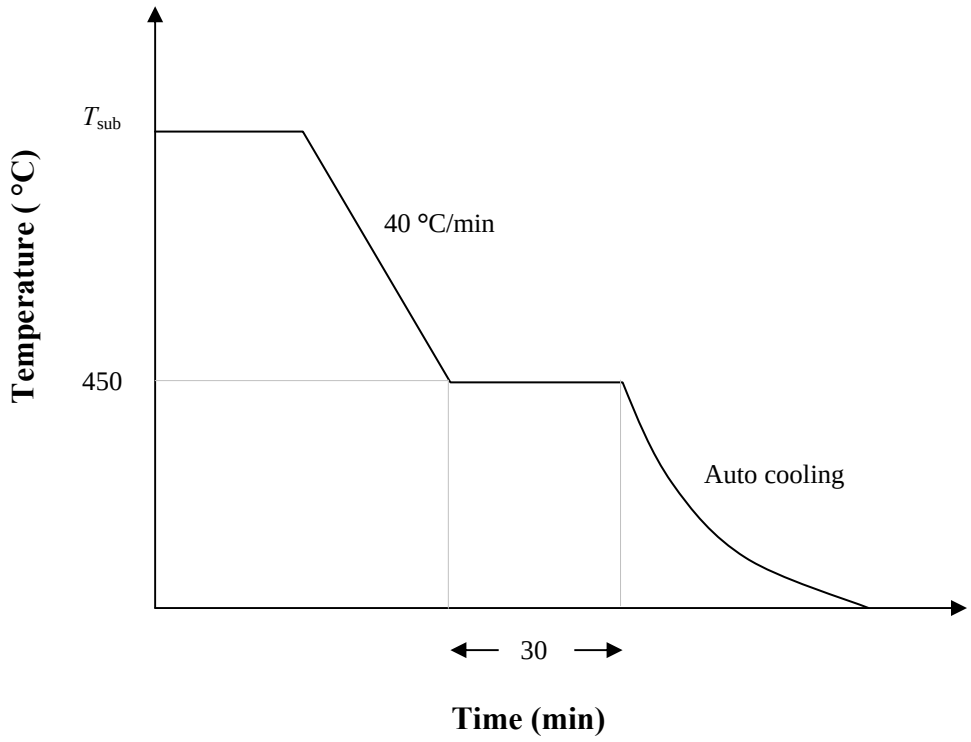

Figure 4.1: Annealing profile - PLD chamber.

4.1.3 Measuring the Critical Temperature (T_c)

- Four gold wires were fixed to the sample to make current and voltage terminals. (Figure 4.2)
- Sample was set in the equipment allowing to supply the current and measure the voltage as shown in Figure 4.3
- Circuit was checked for Ohm's law.
- Inner chamber was filled with He gas and vacuum was kept as a insulating layer.
- Constant applied current was set at 1mA.
- The temperature of He gas was reduced up to 50 K using the refrigerator and again allowed to increase the temperature.

- Data (Voltage and Temperature) were recorded while reducing and increasing the temperature.
- By plotting the curve of Voltage (V) vs Temperature (K), T_c (temperature corresponding to the rapid increase of voltage) was obtained.

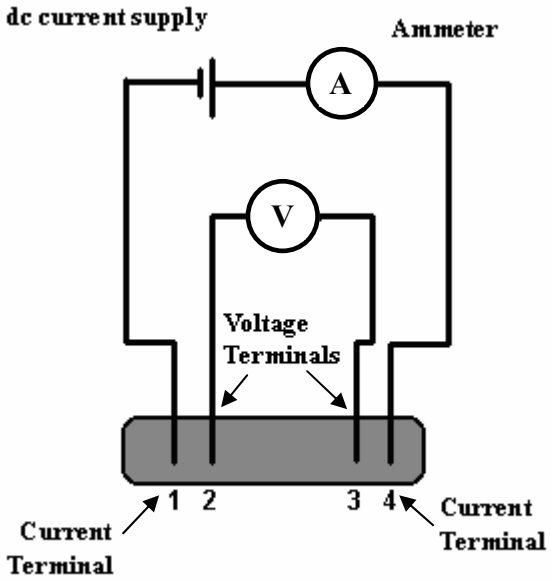

Figure 4.2: Current and voltage terminals of sample.

Figure 4.3: Setting of sample to supply current and voltage.

Figure 4.4: Resistivity measuring machine.

4.1.4 Measuring the Critical Current (I_c)

- Sample patterning with laser etching was done as shown in Figure 4.5

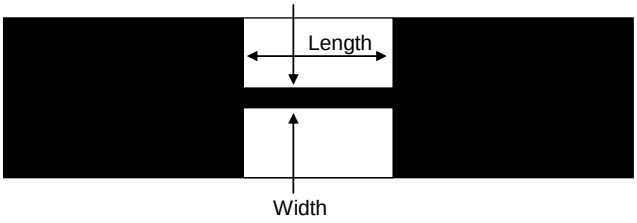

Figure 4.5: Schematic drawing of patterned sample.

Table 4.1: Bridge dimensions of patterned samples

Sample No.	Composition	Current bridge dimension	
		Width [μm]	Length [μm]
1	x=0	108.3	1291.7
2	x=0.3	104.2	1074.1
3	x=0.5	97.4	1229.4
4	x=0.7	116.3	1433.4
5	x=1	112.2	1231.9

- I_c was measured at 77.3 K for narrow bridge in patterned samples using standard four probe method.
- 10 μV/cm criterion was used for these experiments.

4.1.5 Observation of Film Cross –Section

- Film thickness was measured using the cross-sectional images obtained by model JSM-740IF field emission scanning electron microscope (FE-SEM). Prior to the observation samples were prepared as explained in section 3.1.9.

JSM-740IF Field Emission Scanning Electron Microscope (FE-SEM)

This is an ultra high resolution SEM, which employs a field-emission (FE) electron gun as the electron source and a highly excited magnetic objective lens with low aberration. This instrument incorporates the new technologies such as the gentle beam method (GB mode) and r-filter, etc for enabling to control the incident electron exposing the sample surface and the electrons acquired, which are parts of electrons emitted from the sample surface. The development of the gentle beam method, conical objective lens and FE electron gun of conical electrodes type has made it possible to enhance drastically the resolving power of image at low accelerating voltages; this instrument accomplishes the resolution of 1.5 nm at 1 kV accelerating voltage. [1]

Figure 4.6: Model JSM-740IF Field Emission Scanning Electron Microscope (FE-SEM).

4.2 Results and Discussion

4.2.1 Texture Quality

(100) $SrTiO_3$ (STO) single crystal substrates were used to deposit $(Y,H)Ba_2Cu_3O_z$ films because research reports [2,3] have shown that small misfit (Table 1.1) between YBCO and STO single-crystal causes better crystalline quality and developing intrinsic pinning properties.

Highly c-axis oriented thin films were prepared for varying compositions of $(Y_{1-x}Ho_x)Ba_2Cu_3O_z$,x=0, 0.3, 0.5, 0.7 and 1 by optimizing the PLD condition as mentioned in Table 4.2. However, all films contained both "cube-on-cube" and a small amount of "45° rotated" configurations. ("cube-on-cube" configuration is predominant). Figure 4.7 and 4.8 show the XRD θ-2θ and ϕ-scan profiles for x=0.3 sample respectively.

XRD ϕ-scan was conducted around $(Y_{1-x}Ho_x)$BCO (102) planes because in the case of STO substrates, ϕ-scan profile around (103) planes gives only 4 strong peaks with 90° interval due to almost similar lattice parameters of YBCO and STO single crystal [4,5].

Table 4.2: Optimized PLD parameters for $(Y_{1-x}Ho_x)BCO$ films on STO substrates

Composition	x=0	x=0.3	x=0.5	x=0.7	x=1
*Displayed temp. (°C)	840	840	850	857	865
O_2 pressure (Pa)	45	45	45	45	45
T-S distance (cm)	37	37	37	37	37
Energy density (Jcm^{-2})	1.8	1.8	1.8	1.8	1.8
Deposition time (min)	20	20	20	20	20

* The temperature displayed in the PLD machine (T_s is lower than this valve).The relationship between T_s and displayed temperature is not detected yet).

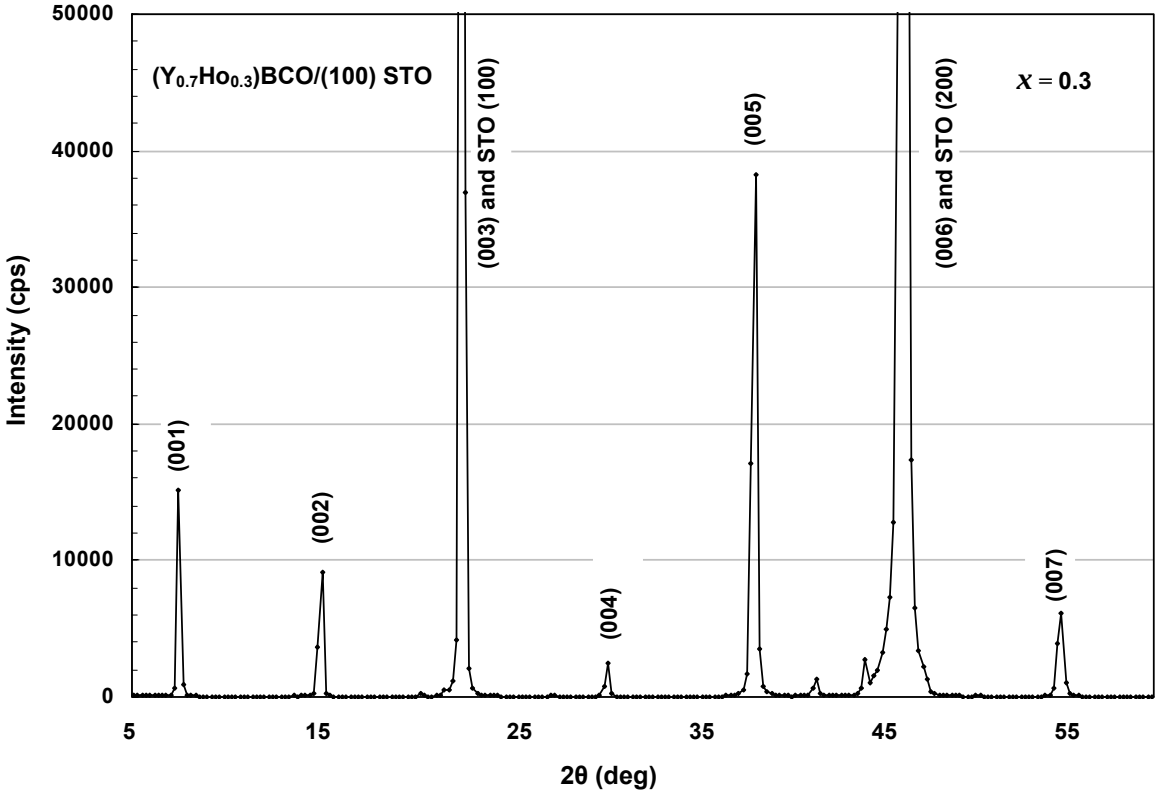

Figure 4.7: XRD: θ-2θ scan for sample x= 0.3.

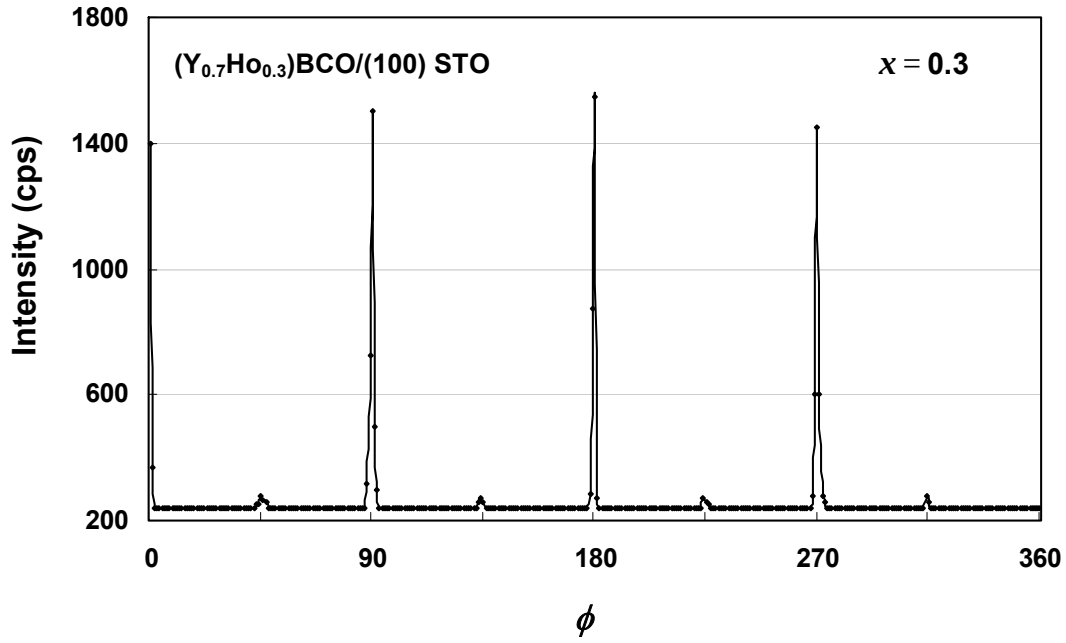

Figure 4.8: XRD ϕ-scan profile for sample of x= 0.3 prepared on STO single crystal substrate.

4.2.2 Critical Temperature Measurements

Temperature dependence of resistivity for ($Y_{1-x}Ho_x$)BCO films deposited on (100) STO single crystal substrates [6-9] are shown in Figures 4.9-4.13. According to the experimental results, T_c valves were obtained in the range of 87-90 K (Table 4.3) under the optimum O_2 annealing condition of 450 ºC at 30 min. Film thicknesses were measured using cross-sectional images (Figure 4.14) obtained by FE-SEM [10] to calculate resistivity. Thicknesses of all films were ranged between 200 nm and 250 nm (Table 4.3), and average film deposition rate was calculated to be 11 nm/min. It was realized that in O_2 annealing [11], annealing temperature and soaking time at that temperature crucially affect the T_c.

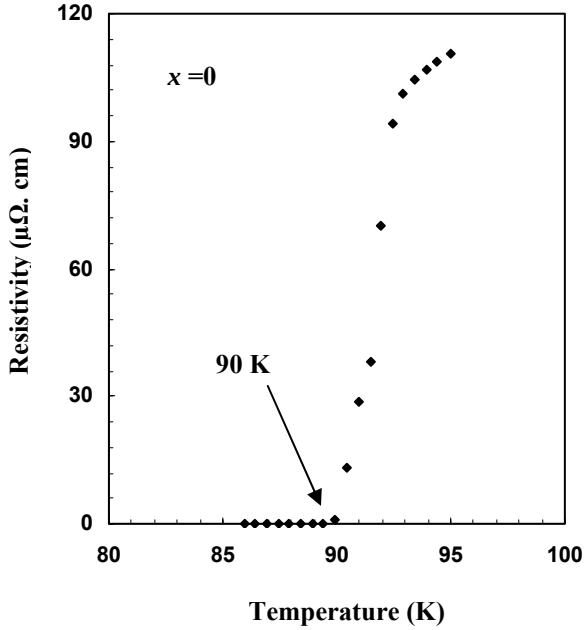

Figure 4.9: Temperature dependence of resistivity for sample x=0

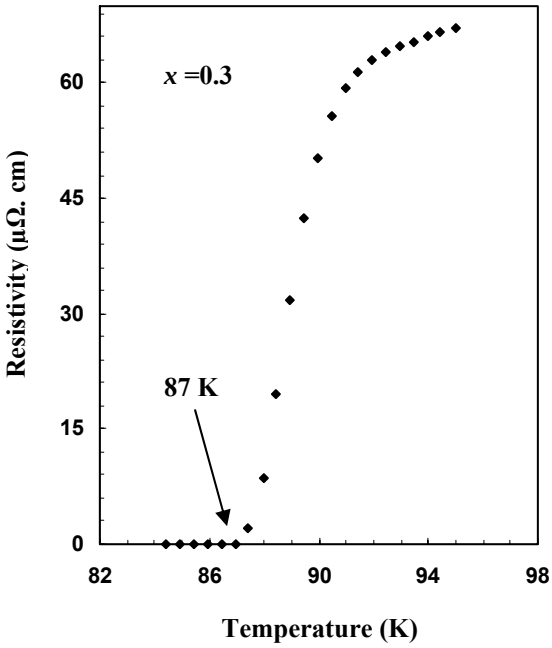

Figure 4.10: Temperature dependence of resistivity for sample x=0.3.

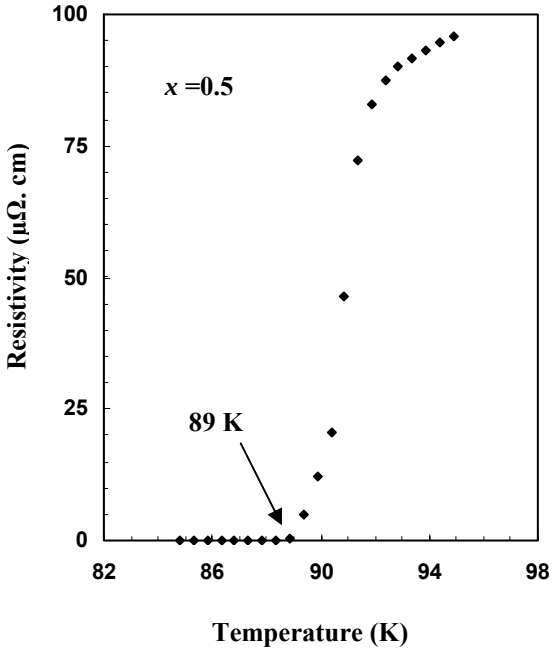

Figure 4.11: Temperature dependence of resistivity for sample x=0.5.

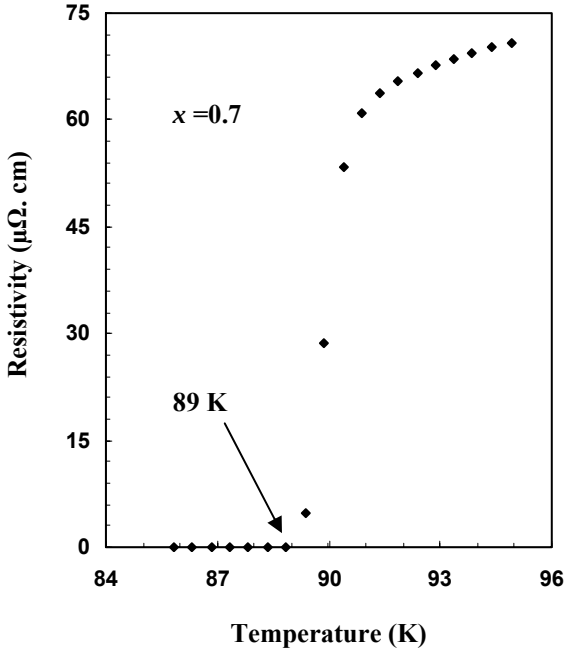

Figure 4.12: Temperature dependence of resistivity for sample x=0.7.

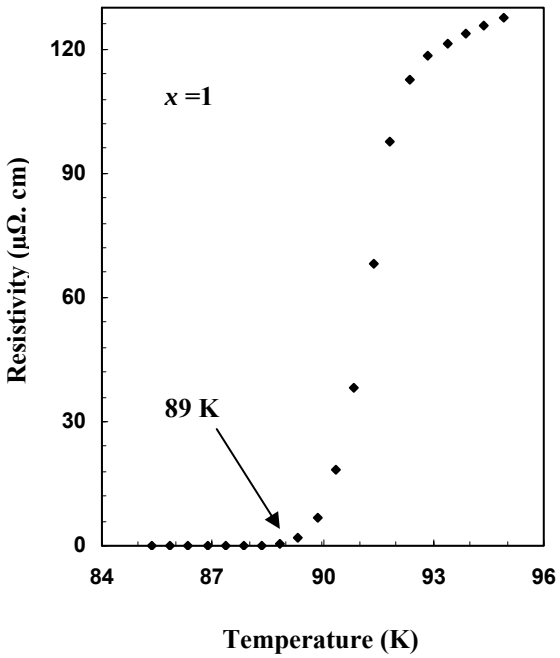

Figure 4.13: Temperature dependence of resistivity for sample x=1.

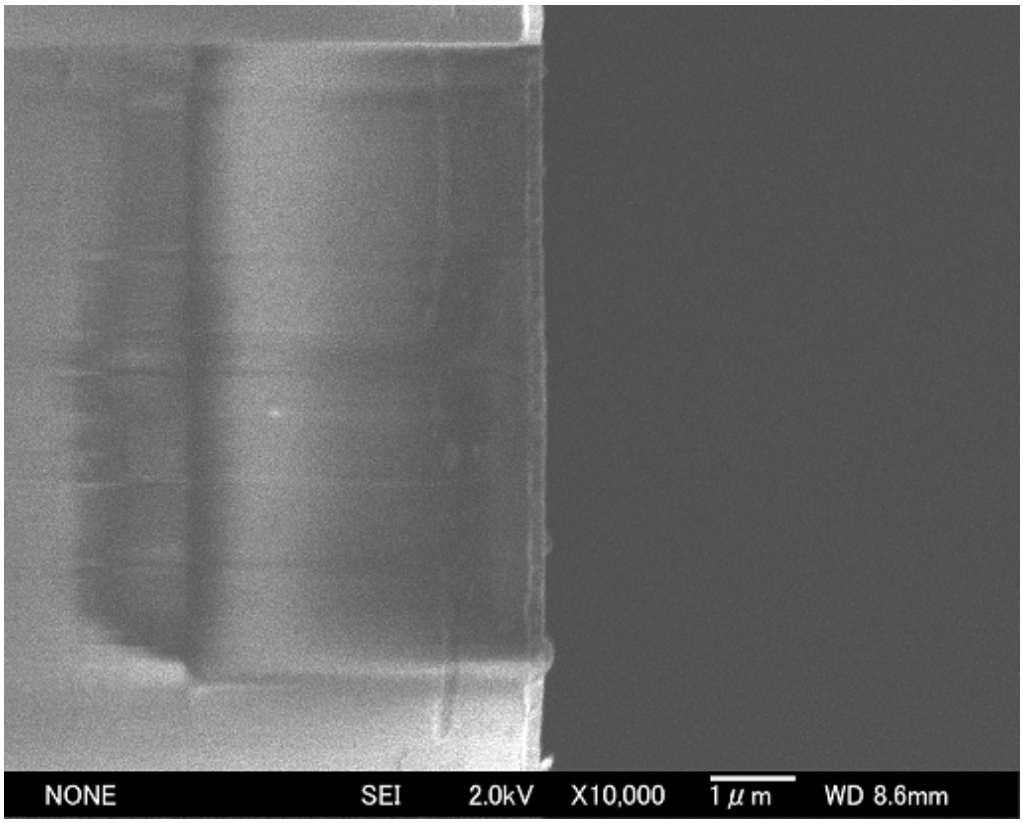

Figure 4.14: FE-SEM cross-sectional image of sample x=0.3.

Table 4.3: T_c and thickness for $(Y_{1-x}Ho_x)BCO$ films on STO substrates.

Composition	$x = 0$	$x = 0.3$	$x = 0.5$	$x = 0.7$	$x = 1$
T_c (K)	90	87	89	89	89
Thickness (nm)	250	200	200	250	200

4.2.3 Critical Current Density Measurements

I_c and J_c of $(Y_{1-x}Ho_x)$BCO films deposited on (100) STO single crystal substrates are shown in Table 4.4.

Table 4.4: I_c and J_c of $(Y_{1-x}Ho_x)$BCO films on STO substrates.

Composition	$x = 0$	$x = 0.3$	$x = 0.5$	$x = 0.7$	$x = 1$
I_c (mA) ;77.3 K, self field	310	316	27	367	186
J_c MA/cm^2	1.20	1.45	0.14	1.26	0.83

The J_c in epitaxial REBCO films strongly depends on the film thickness. Several reports reveal that the nanostructure of pulsed laser deposited epitaxial REBCO films is evolving during growth due to high dislocation mobility and this results in degrading the J_c with higher film thickness [12,13]. Therefore in this work attention was paid to fabricate films with lower thickness and those were ranged between 200 nm and 250 nm.

J_c values were measured to be at around 1 MA/cm^2 (0.8-1.5 MA/cm^2) except for x=0.5. This extremely low J_c of x=0.5 could be caused by some experimental error such a failure in oxygen annealing. The highest J_c value was about 1.5 MA/cm^2 for the film of x=0.3. However these results showed that J_c has no an exact relationship with Y:Ho ratio as can be seen in figure 4.15.

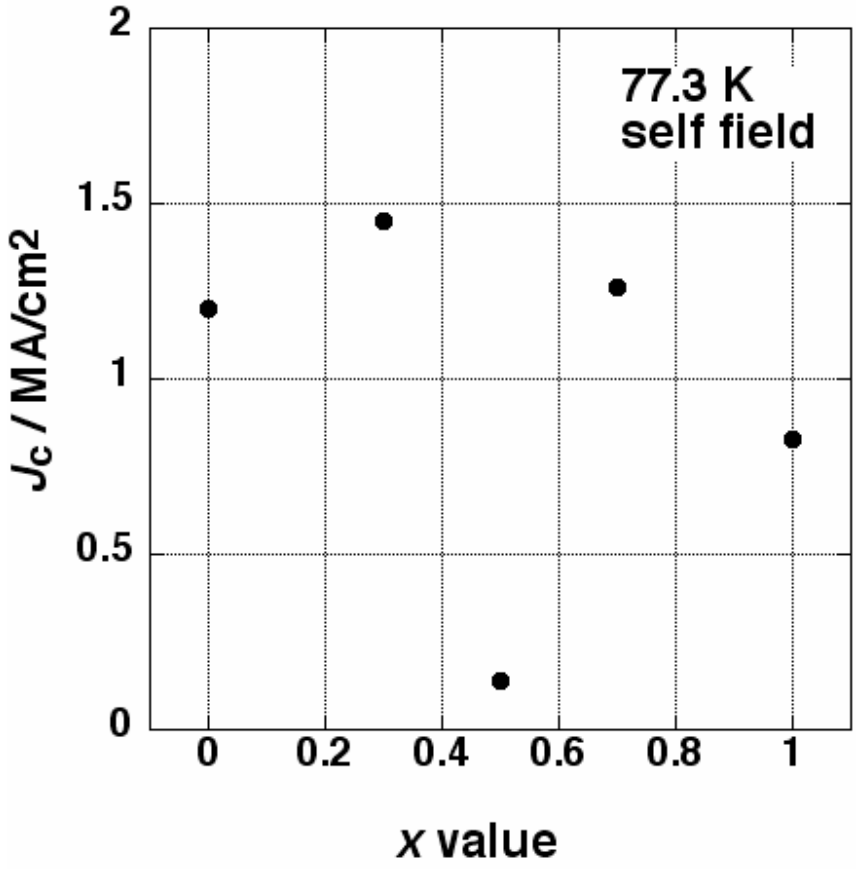

Figure 4.15: Y/Ho ratio dependence of critical current density (J_c).

4.3 References

(1) JSM-740IF field emission scanning electron microscope operating guide (2004).

(2) T. Horide, K. Matsumoto, K. Osamura, A. Ichinose, M. Mukaida, Y. Yoshida, S. Horii, Physica C 412–414, 1291–1295 (2004).

(3) J. Gutierrez, A. Llordes, J. Gazquez, M. Gibert, N. Roma, S. Ricart, A. Pomar, F. Sandiumenge, N. Mestres, T. Puig, X. Obradors: Nat. Mater. **6,** 367 (2007).

(4) K. Kim, M. Paranthaman, D.P. Norton, T.Aytug, C.Cantom, A.A. Gapud, A. Goyal, D.K.Christen, Supercond. Sci. Technol. 19, R23–R29 (2006).

(5) H. Dai, S. Yoon, J.Liu, R.C. Budhani, C.M.Lieber, Science, 265, 1552-1555 (1995).

(6) R. Wordenweber, Supercond. Sci. Technol. 12, R86–R102 (1999).

(7) G.P. Summers, E.A. Burke, D.B. Chrisey, M. Nastasi, J.R. Tesmer, Appl. Phys. Lett. 55,1469 (1989).

(8) C.V. Varanasi, P.N. Barnes, J. Burke, L. Brunke, I.Maartense, et al. Supercond. Sci. Technol. 19, L37 (2006)

(9) T.A. Campbell, T.J. Haugan, I. Maartense, J. Murphy, L. Brunke, P. Barnes, Physica C 423 (2005).

(10) JSM-740IF Field Emission Scanning Electron Microscope Operating Guide, 2004.

(11) M.Ohmukai, T.Fujita, T.Ohno, Brazilian Journal of Physics, 31, 1,(2001).

12) Y.V. Cherpak, V.L. Svetchnikov, A.V. Semenov, V.O. Moskaliuk, C.G. Tretiatchenko, V.S. Flis, V.M. Pan, Journal of Physics: EUCAS 2007, 97, 012259 (2008).

13) Y.V. Cherpak, V.O. Moskaliuk, A.V. Semenov, V.L. Svetchnikov, C.G. Tretiatchenko, V.M. Pan, Supercond. Sci. Technol. 20, 1159–1164 (2007).

CHAPTER 5

Conclusions and Future Prospects

5 Conclusions and Future Prospects

Second generation high temperature superconducting wires (2G) based on the REBCO coated conductor have been under development world-wide and that is on the way to commercial application. In this study improved Q-switched Nd:YAG pulse laser was applied to the PLD process with the ultimate objective of fabrication of cost-effective coated conductors. In producing coated conductors from the high temperature superconducting compounds, REBCO, biaxial crystallographic texture is necessary to optimize current carrying properties because high angle grain boundaries act as 'weak links' and substantially reduce the J_c. Using fourth harmonic Nd:YAG pulse laser (266 nm UV radiation), highly biaxially textured (Y,Ho)$Ba_2Cu_3O_z$ films were successfully prepared on (100)MgO and (100)STO single-crystal substrates optimizing the PLD parameters.

According to the experimental results, there was no change in lattice constants of $(Y_{1-x}Ho_x)Ba_2Cu_3O_z$ with Y:Ho ratio. Further it was revealed that Y:Ho ratio does not cause obvious changes in texture quality. This is because the ionic radius of Y^{3+} is almost similar to that of Ho^{3+}.

This study showed, T-S distance with oxygen pressure and with laser energy density have specific interrelated effects on the texture quality of the films. Within our experimental setup; p values of 20 and 22 Pa with d_{TS} value of 45 mm, and E of 2 Jcm^{-2} with d_{TS} of 45 mm were selected as the most effective combinations for the preparation of c-axis oriented YBCO (x=0) films. Further, it was revealed that relative to the effects of other PLD parameters, T_{sub} crucially affected the preparation of c-axis oriented films with improved in-plane texture and should be increased with the Ho content.

For (Y,Ho)$Ba_2Cu_3O_z$ films deposited on (100) STO single crystal substrates, T_c values were obtained just below 90 K which are thought to be practically sufficient values. It was concluded that oxygen annealing temperature and soaking time

greatly affect the T_c and those were set at 450^0C and 30 min., respectively to achieve the optimum annealing condition. Further investigations are required to find the relationship between T_c and oxygen pressure.

J_c values were measured to be around 1 MA/cm^2 (0.8-1.5 MA/cm^2) except for x=0.5. The highest J_c value was about 1.5 MA/cm^2 for the film of x=0.3. This value is not so high value at present. Therefore it is recommended to improve the Q-switched Nd:YAG pulse laser adjusting the energy level up to second and third harmonic types (wavelengths of 532nm and 355nm respectively). In addition to that attention should be directed to adjust the pulse repetition rate and pulse duration (FWHM) of Nd:YAG lasers in order to enhance the quality of laser (In this study pulse repetition rate and pulse duration (FWHM) were set at 10 Hz and 18 ns respectively).

In present study, significant enhancement in J_c of (Y,Ho)$Ba_2Cu_3O_z$ was not observed and there was no an exact relationship between the Y:Ho ratio and J_c . It seems that different electron potential energies in randomly distributed Y^{3+} and Ho^{3+} sites do not have strong effect on flux pinning. Therefore REBCO films containing multiple rare-earth elements with different ionic radii ((RE,RE')$Ba_2Cu_3O_z$) are taken into consideration to investigate flux-pinning behavior. The effect of the combination of compositional randomness and APCs of nano-rods (As example, $BaZrO_3$; BZO) on improving flux-pinning is investigated because we could not find reports regarding this. As an initial step thin films of $(Eu_{0.7}Gd_{0.3})Ba_2Cu_3O_z$ and $(Eu_{0.7}Gd_{0.3})Ba_2Cu_3O_z$ + 2 weight % BZO were deposited on (100) MgO single crystals using Nd:YAG laser at 266 nm. For both compositions, T_c was measured as around 90 K. TEM observations are carried out to examine the nanorods after determining the J_c.

Although, many reports are available regarding the improvement of J_c introducing various types of nano-particles ($BaZrO_3$, $BaSnO_3$ and Y_2O_3 etc.); the

most effective particle type, size and introducing method are still not revealed. This is a remaining task for materials scientists who work for development of coated conductors.

J_c has been found to decrease with increasing REBCO film thickness. But Thicker high-quality REBCO films with high critical currents need to be developed because HTS coated conductors with such films will be able to transport large amounts of current suitable for electric power applications. In present research, even though, films were fabricated with lower thickness of 200-250 nm, this is not the optimum thickness which corresponds to the maximum J_c. Therefore it is recommended to study the influence of film thickness on J_c with the aim of finding optimum film thickness of REBCO films. Average film deposition rate was calculated to be 11 nm/min which is relatively low value. However, challenges remain in maintaining the outstanding HTS properties of coated conductors while increasing film deposition rates on longer tape lengths. Real time monitoring and control is needed to reduce grain boundaries, mis-orientations, and defects that can decrease the current carrying capabilities of coated conductors.

REBCO epitaxial films are abundant in various defects and surface particles/precipitates due probably to their complexity in chemical compositions and crystal structures. Particle densities of the $(Y_{1-x}Ho_x)Ba_2Cu_3O_z$ films prepared in this work were nearly the same as the PLD-YBCO films fabricated using an excimer laser. Among these samples, x=0 (YBCO) and x=1 (HoBCO) seems to have slightly lower particle densities relative to others, but exact reason for this difference has not been revealed yet. Systematic investigation of particle formation on the film surface can be carried out to find the reason and it would be helpful to further suppress the formation of particles. Especially it should be mentioned that particle generation which is frequently pointed out as a characteristic problem of

Nd:YAG-PLD was remarkably suppressed, even though that is practically insignificant for the purpose of coated-conductor application.

Present results shows that Nd:YAG-PLD could be one of a hopeful process for fabrication of cost-effective coated-conductors with improved current characteristics.

List of Publications and Conferences

Publications

(1) G. I. P. De Silva, T. Maeda, "Pulsed Laser Deposition of Oxide Superconductor Films Using Fourth Harmonics of Nd:YAG Laser at 266 nm", Mater. Sci. Tech. (Accepted).

(2) G.I.P. De Silva, T. Maeda, S. Horii, Y. Ichino and Y. Yoshida, **"**Application of Nd:YAG Laser to Fabricate Oxide Superconductor Films for Coated Conductors", Journal of Physics: European Conference on Superconductivity (EUCAS 2009), Dresden, Germany (Submitted).

Conferences

(1) G.I.P De Silva, T. Maeda, "Texture Analysis of (Y,Ho)$Ba_2Cu_3O_z$ (z~7) Films Prepared by means of Pulsed-Laser-Deposition Method", 20^{th} International Symposium on Superconductivity, Tsukuba, Japan, November 5-7, 2007.

(2) G.I.P De Silva, T. Maeda, "Analysis of Texture Quality and Current Characteristics of (Y,Ho)$Ba_2Cu_3O_z$ (z~7) Thin Films Produced By Pulsed Laser Deposition Method", International Union of Materials Research Societies (IUMRS) Conference, Nagoya, Japan, December 9-13,2008.

(3) G.I.P De Silva, T. Maeda, "Characterization of (Y,Ho)BCO Films Fabricated by Forth Harmonic Nd:YAG Pulsed Laser Deposition", Cryogenic Society of Japan (CSJ) Conference, Vaseda, Japan, May 13-15, 2009.